Coordination Chemistry Reviews 407 (2020) 213156

Contents lists available at ScienceDirect

Coordination Chemistry Reviews

journal homepage: www.elsevier.com/locate/ccr

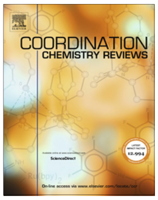

Review

Prussian blue analogues and their derived nanomaterials for electrocatalytic water splitting

Li-Ming Cao [a,b], David Lu [a], Di-Chang Zhong [a,*], Tong-Bu Lu [a,*]

[a] *Institute for New Energy Materials & Low Carbon Technologies, School of Materials Science and Engineering, School of Chemistry and Chemical Engineering, Tianjin University of Technology, Tianjin 300384, China*
[b] *College of Chemistry and Chemical Engineering, Jiangxi Normal University, Nanchang 330022, China*

ARTICLE INFO

Article history:
Received 19 May 2019
Accepted 13 December 2019

Keywords:
Prussian blue analogue
Water splitting
Electrocatalyst
Nanomaterial
Metal-organic framework

ABSTRACT

The electrocatalytic water splitting is considered as a prospect meaning to address the urgent energy and environmental problems. However, the electrocatalytic water splitting is greatly limited by the high overpotentials of hydrogen evolution reaction (HER) and oxygen evolution reaction (OER). Especially, OER involves a complex multistep proton-coupled electron transfer process, which demands a high overpotential to accelerate this sluggish oxygen evolution kinetics. The high overpotentials for OER significantly decrease the efficiency of the overall water splitting. The OER half reaction has thus become the bottleneck of electrocatalytic overall water splitting. It is vital to synthesize highly active electrocatalysts to reduce the activation energy of the reaction and accelerate the generation of H_2 and O_2, thereby improving the efficiency of the overall water splitting. Prussian blue analogues (PBAs) are representative cyanide-based coordination polymer materials. PBAs possess open framework structures, large specific surface areas, adjustable metal active sites and uniform catalytic centers, showing promising application in electrocatalytic water splitting. Besides, benefiting from the unique structural features of PBAs, their derived electrocatalysts also have large specific surface areas and uniform active sites. Moreover, PBAs can serve as carbon and nitrogen sources. The doped N can regulate the electronic structure of surface active sites, enhancing the intrinsic activity of electrocatalysts. Therefore, the PBA-derived electrocatalysts also exhibit good catalytic performance for water splitting. In this review, we not only summarize the most recent advances on PBAs and their derivatives as electrocatalysts for water splitting, but also conclude the core scientific challenges faced in water splitting. Finally, we provide perspectives for the future research in this field, including catalyst design, catalytic system establishment and so on.

© 2019 Elsevier B.V. All rights reserved.

Contents

---

* Corresponding authors.
E-mail addresses: zhong_dichang@hotmail.com (D.-C. Zhong), lutongbu@tjut.edu.cn (T.-B. Lu).

https://doi.org/10.1016/j.ccr.2019.213156
0010-8545/© 2019 Elsevier B.V. All rights reserved.

1. Introduction

With the rapid development of the global economy, the increasingly depleted traditional fossil fuels will not meet the growing energy needs of mankind [1]. In addition, the burning of fossil fuels leads to excessive emissions of greenhouse gases. Carbon dioxide (CO_2), the main greenhouse gas, triggers a series of serious environmental problems such as global warming and melting glaciers [2]. These energy crisis and environmental problems greatly threaten the sustainable development of mankind. Therefore, it is extremely urgent to find renewable energy sources. Hydrogen (H_2), with a high calorific value and a clean combustion product, is an ideal renewable clean energy source [3]. Among hydrogen producing protocols, water splitting has been considered as one of the most promising technology due to its sustainability and environmental-friendly [3]. Water splitting can be drived by light and electricity. In photocatalytic water splitting, the photocatalyst absorbs sunlight to generate photogenerated electrons and holes, which transfer to H_2O molecule and lead to the splitting of water into H_2 and O_2 [4,5]. The photocatalytic water splitting is the most ideal method to obtain H_2, as the solar energy is an inexhaustible renewable energy source. However, despite tremendous efforts of researchers during the past several decades, this technology still suffers from many shortcomings including low conversion efficiency, high conversion costs, and unstable catalysts, which limit its large-scale development [4,5]. In electrocatalytic water splitting, the electric energy drives the decomposition of water to produce H_2 and O_2, which is a process of directly converting electrical energy into chemical energy. In contrast to the photocatalytic water splitting, the electrocatalytic water splitting possesses higher conversion efficiency, and can obtain higher-purity H_2 [6,7]. In addition, the electrical energy can be steadily provided, and readily transferred from renewable energy sources such as wind, solar and tidal energy [8]. As a consequence, electrocatalytic water splitting is a more practical strategy to convert renewable energy into hydrogen energy and has been highly concerned by researchers.

The electrocatalytic water splitting consists of two half-reactions: hydrogen evolution reaction (HER) and oxygen evolution reaction (OER) [6,7]. These two half reactions differ depending on the electrolytes of the water splitting reaction [3,7].

In acidic media:

$$\text{HER: } 2H^+ + 2e^- \rightarrow H_2$$

$$\text{OER: } H_2O \rightarrow 2H^+ + 1/2O_2 + 2e^-$$

In neutral and alkaline media:

$$\text{HER: } 2H_2O + 2e^- \rightarrow H_2 + 2OH^-$$

$$\text{OER: } 2OH^- \rightarrow H_2O + 1/2O_2 + 2e^-$$

The reported catalysts usually have much less tolerant in acid media than in alkaline media. Normally, the HER involves three possible reaction steps [3,7].

Volmer step

$$H^+ + e^- \rightarrow H_{ads} \text{ (in acidic media)}$$

$$H_2O + e^- \rightarrow H_{ads} + OH^- \text{ (in alkaline media)}$$

In this reaction, electrons are shifted to the electrode surface to snatch proton in solution, generating the intermediate state of adsorbed hydrogen atoms (H_{ads}) on the catalytic active sites. There are two different pathways to obtain hydrogen in the subsequent step. When the adsorbed hydrogen atoms have a low coverage, which are inclined to couple with new electron and proton to generate hydrogen [3,7].

Heyrovsky step

$$H_{ads} + H^+ + e^- \rightarrow H_2 \text{ (in acidic media)}$$

$$H_{ads} + H_2O + e^- \rightarrow H_2 + OH^- \text{ (in alkaline media)}$$

However, when the H_{ads} coverage is high, the recombination of adjacent H_{ads} will dominate, resulting in the following chemical desorption reaction, also known as Tafel reaction [3,7].

Tafel step

$$H_{ads} + H_{ads} \rightarrow H_2$$

At present, most bifunctional catalysts for water splitting work in alkaline media. That is to say, the alkaline media facilitates electrocatalytic oxygen release. Generally, the OER involves four proton-coupled electron transfer (PCET) process. In acidic electrolyte, the involved process can be presented as follows [7,9]:

$$H_2O + * \rightarrow OH^* + H^+ + e^-$$

$$OH^* \rightarrow O^* + H^+ + e^-$$

$$O^* + H_2O \rightarrow OOH^* + H^+ + e^-$$

$$OOH^* \rightarrow O_2 + * + H^+ + e^-$$

where * stands for the active sites of electrocatalysts. In alkaline electrolyte, the catalytic reaction can be expressed as follows [7,9]:

$$OH^- + * \rightarrow OH^* + e^-$$

$$OH^* + OH^- \rightarrow O^* + H_2O + e^-$$

$$O^* + OH^- \rightarrow OOH^* + e^-$$

$$OOH^* + OH^- \rightarrow O_2 + * + H_2O + e^-$$

The practical application of electrocatalytic water splitting is mainly limited by the high overpotentials of HER and OER [6,7,10]. Especially, the OER involves a complex multistep proton-coupled electron transfer (PCET) process, resulting in sluggish oxygen evolution kinetics, which requires a high overpotential to accelerate the reaction [6,7,10]. The high overpotentials for OER significantly reduce the efficiency of the overall water splitting, which in turn hinders the efficiency of H_2 formation [6,7,10]. The

OER thus becomes the bottleneck in electrocatalytic water splitting. It is important to prepare highly active electrocatalysts to reduce the activation energy of the reaction and accelerate the generation of H_2 and O_2, thereby improving the efficiency of the overall water splitting.

An excellent electrocatalyst for water splitting should combine the superiorities of low cost, high efficiency and high stability. In other words, the design and synthesis of catalysts should obey the following rules [7]: (1) driving large current density for water splitting at low overpotentials; (2) endurance for a wide pH range; (3) excellent stability for up to several years; (4) cheap raw materials and simple synthesis methods. At present, Pt-group metals, Ir- and Ru-based compounds are the state-of-the-art catalysts for electrocatalytic water splitting [11]. However, the scarcity and high cost of these metal catalysts have seriously hindered their large-scale commercial application. Therefore, it is much desired to develop low-cost, readily available and highly active water splitting catalysts. The abundant transition metals involving Fe, Co, Ni, Cu, Mo and Cu, etc. spontaneously enter in the researchers' views [6,7,12]. These metals possess good redox properties, and their properties can be improved by modification of the environments around them [6,7,12]. Therefore, transition metals with variable valences have attracted considerable interest in water splitting catalysts design.

The design of electrocatalysts for water splitting is different in acidic and alkaline electrolytes. The strong corrosive nature of the acidic medium can lead to a serious decline in the stability of catalysts [13]. Therefore, the design and synthesis of catalysts used in acidic media should pay attention to their resistance to strongly acidic electrolytes. Carbon-based nanomaterials have attracted extensive attention in water splitting due to the excellent corrosion resistance of carbon [13]. Precisely adjusting the coating of the carbon layer on the catalysts can effectively avoid the exposure of the catalysts in the strongly acidic electrolytes, thereby improving the stability of the catalysts. In particular, design and synthesis of graphite carbon coated catalysts can improve conductivity and stability. Therefore, fabricating non-precious metal carbon-based nanomaterials may be a good means to get water-splitting catalysts suitable for acidic media. The vast majority of catalysts are well tolerated in alkaline media, so for the design and synthesis of such catalysts, more efforts should be focused on the improvement of their intrinsic activity by regulating the electronic structure of the catalytic center [2,6,7]. For example, element doping and adjustment of coordination configuration are effective methods for controlling the electronic structure of the active center [2,6,7]. To date, great efforts have been devoted to the developments of non-precious metal-based electrocatalysts working in acidic or basic conditions.

The non-precious metal-based eletrocatalysts for water splitting mainly include homogeneous molecular complexes [12] and heterogeneous metal oxides, hydroxides, sulfides, selenides, phosphides, carbides, nitrides, borides [14–19]. Overpotential, Tafel slope, Faradaic efficiency, etc. are important parameters to evaluate the catalytic activity of these water-splitting electrocatalysts. Overpotential (η) is an extra potential that beyond the theoretical potential of an electrochemical reaction, which is an additional driving force to overcome dynamic obstacles during the catalytic conversion process [3]. Overpotential at a current density (j) of 10 mA cm^{-2} is often used to evaluate the activity of an electrocatalyst [7]. In a photoelectrochemical (PEC) cell, solar-to-hydrogen (STH) efficiency can be calculated by Eq. (1) [20].

$$STH = (j \times E_c \times Q)/P \tag{1}$$

where j is the current density without any external applied bias, E_c is the thermodynamic reversible water electrolysis cell voltage at 1.23 V, Q is the Faradaic efficiency for water splitting, P is the solar irradiation power density on earth at "Air Mass 1.5 Global". Here, a 10 mA cm^{-2} current density for electrochemical water splitting indicates a 12.3% STH efficiency (presuming the Faraday efficiency of cell is unity) [21–24]. The lower the overpotential value, the better the catalytic activity. Tafel slope is calculated from the Tafel plots which are usually got through replotting the linear sweep voltammogram (LSV) as plots of log(j) versus overpotential [3,7]. The Tafel slope can then be obtained via fitting the linear portion of Tafel plots to Eq. (2).

$$\eta = b\log(j/j_0) \tag{2}$$

where b is the Tafel slope, j is the current density, and j_0 is the exchange current density [3]. The smaller Tafel slope suggests the faster charge transfer kinetics of the electrocatalyst. The exchange current density is always utilized as a parameter to evaluate catalyst activity, especially for HER catalysts. The kinetics of HER exceed the defined overpotential of the catalyst, thus almost all catalysts possess similar kinetics in HER, meaning the exchange current density is directly related to the onset overpotential in HER. Therefore, it can be utilized as an activity parameter [7]. The electrochemical surface area (ECSA) reflects the inherent catalytic performance of catalysts. ECSA can be estimated by measuring the electrochemical double-layer capacitances (C_{dl}) [25,26]. The potential range of CV locating at non-Faradaic region was chosen. And the different sweep rates were chosen. A linear was achieved by plotting the measured capacitive currents against the sweep rates. The C_{dl} is half of the linear slope, which was used to represent the ECSA. Faradaic efficiency, illustrating the efficiency that electrons supplied by an external circuit shift to drive an electrode reaction, is a significant parameter for evaluating the selectivity and activity of electrocatalysts [27–29]. Faradic losses will appear when byproducts or heat of the electrode reaction are formed. In water splitting, the practical yielding H_2 and O_2 can be determined by gas chromatography. The theoretical output can be calculated from galvanostatic or potentiostatic electrolysis by integration. Faradaic efficiency is the ratio of practical and theoretical yield [7,9]. Turnover frequency (TOF) is defined as the number of conversion reaction per catalytic active site per unit time [21], which is also important index to illustrate the catalyst activity. Generally, the TOF values can be calculated by Eq. (3).

$$TOF = j/(4 \times F \times n) \tag{3}$$

where j is the current density (mA cm^{-2}), F is the faraday constant (96485C mol^{-1}), n is moles of electrocatalysts (mol cm^{-2}) [28].

In addition to the above mentioned electrochemical indexes, stability is also an important index determining the possible practical application of an electrocatalyst. The stability of catalysts can be measured by cyclic voltammetry (CV) and galvanostatic or potentiostatic electrolysis [3]. After hundreds of CV cycles, under the same current density, the less the overpotentials increase, the higher durability of the catalysts possess. In galvanostatic or potentiostatic electrolysis, the stability of catalysts is measured at a fixed current density or potential.

Several strategies have been developed to prepare highly active catalysts for water splitting. (1) Engineering the electronic structure of surface active sites by structural modification or elemental doping could effectively enhance the intrinsic activity of the electrocatalyst [2,6,7]. (2) Modulating the morphology of electrocatalyst to increase the active sites and specific surface area will also beneficial for the enhancement of the catalytic activity [2,6,7,27]. (3) Combining the catalyst with a conductive substrate (graphene, carbon nanotube, Ni foam, etc.) to facilitate the charge transfer from the conductive carrier to electrocatalyst surface, has also been evidenced as an effective means to enhance the catalyst activity [2,18].

Porous coordination polymers (PCPs, also called metal-organic frameworks (MOFs)) are a class of structurally ordered crystalline materials formed by self-assembly of metal ions or clusters with organic ligands [30–33]. PCPs have high specific surface areas, high levels of porosity, adjustable structure, and multiple active sites, which are widely used in gas separation and storage, catalysis, molecular sensing and drug release [30–39]. Recently, PCP-based materials, including the pristine PCPs and their derived porous nanomaterials, have demonstrated to be electrocatalysts for water splitting [30,40–44]. For example, $[Co_2(\mu\text{-}Cl)_2(btta)]$(MAF-X27-Cl, H_2bbta = 1H,5H-benzo(1,2-d:4,5-d)bistriazole) only required an overpotential of 290 mV to obtain a 10 mA cm^{-2} current density in 1.0 M KOH [33]. The ultrathin NiCo bimetal-organic framework nanosheets (NiCo-UMOFNs) only demanded overpotentials of 250 mV and 189 mV to obtain the 10 mA cm^{-2} current density in 1.0 M KOH on a glassy-carbon electrode and copper foam [43]. In addition to the pristine MOFs, MOF derivatives have also been used for electrocatalytic water splitting [45–49]. The MOF-derived electrocatalysts not only retain the original structural characteristics of MOFs, but also have large specific surface areas and uniform active sites. Furthermore, in-situ generated graphite carbon can improve the conductivity and stability of the electrocatalysts [45–49]. Thus, MOF derivatives always exhibit enhanced electrocatalytic performance. For instance, Co-naphthalenedicarboxylate MOF derived Co_3O_4-carbon porous nanowire arrays showed outstanding electrocatalytic performance for OER [47]. The zeolitic metal azolate framework MAF-6 as a template carbon-coated WC nanoclusters only required an overpotential of 51 mV to drive a current density of 10 mA cm^{-2} for HER in 0.5 M H_2SO_4 [48]. ZIF-67 derived Co-P/NC electrocatalyst exhibited great electrochemical activity for both OER and HER, which demanded overpotentials of 319 mV and 154 mV to obtain the 10 mA cm^{-2} current density in 1.0 M KOH, respectively. Moreover, the Co-P/NC-based electrolyzer only demanded a cell voltage of 2.0 V to drive a current density of 165 mA cm^{-2} for overall water splitting [49]. Although the research of MOF-based electrocatalysts for water splitting has made some progress, their catalytic performance is still a long way from meeting the requirements of commercialization.

Prussian blue (PB) and Prussian blue analogues (PBAs), are representative cyanide-bridged coordination polymers generated by the reactions of metal ions with transition-metal cyanometalates, which have a face-centered cubic structures with the following formula: $A_xM_A[M_B(CN)_6]_y \cdot zH_2O$, where A is the cations intercalated between the frameworks, M_A and M_B are the metal ions coordinated to the cyano groups [50–60]. The earliest synthetic report for PB dates back to the early 18th century [61]. PB was made by a German with ash, bovine blood and ferric chloride, and was originally used as a dye. Since the first synthesis of this pigment was done in Berlin, the Kingdom of Prussia, it is called Berlin Blue, or more commonly Prussian Blue [62]. Later chemical characterization confirmed that PB was a complex of iron cyanide. PBAs not only have nanoporous open framework structures and large specific surface areas, but also own the advantages of low cost and easy preparation [50,51]. Due to the adjustable metal active sites and uniform catalytic centers, PBAs have been found promising application in electrocatalytic water splitting [63–66]. For example, Co-Fe Prussian blue coordination polymer exhibited great electrocatalytic performance for OER [65]. A Ni-Fe PBA thin film showed good electrocatalytic activity for HER, requiring an overpotential of 200 mV to obtain the 10 mA cm^{-2} current density in 1.0 M KOH. Moreover, the Ni-Fe PBA thin film and Co-Fe PBA thin film could act as cathode and anode to fabricate an electrolyzer for overall water splitting. In addition, PBAs have also been demonstrated to be promising templates/precursors for the preparation of nanomaterials [67–72]. Benefiting from the unique structural features of PBAs, their derived electrocatalysts have large specific surface areas and uniform active sites. Besides, PBAs have abundant carbon and nitrogen sources, the in-situ formed carbon can promote electron conduction and stabilize the electrocatalysts. The doped N can regulate the electronic structure of surface active sites, offering more adsorption sites for H*, enhancing the intrinsic activity for HER. Therefore, these PBA-derived electrocatalysts exhibited good catalytic performance for water splitting [68,69]. For example, Chen et al. prepared FeCo alloy nanoparticles coated in N-doped graphene layers via carbonization of Fe-Co PBA [68]. The derived N-doped graphene layers coated FeCo alloy nanoparticles exhibited a onset overpotential of 88 mV for HER and required an overpotential of 262 mV to obtain the 10 mA cm^{-2} current density in 0.5 M H_2SO_4. In addition, PBA ($M_3[Co(CN)_6]_2$) derived $M_xCo_{3\text{-}x}O_4$ (M = Co, Mn, Fe) porous nanocages showed great catalytic activity for OER in phosphate buffer solution (pH = 7) [69].

Although the researches on catalysts for electrocatalytic water splitting have made great progress, there are still many challenges [6,7]: (1) Accurate synthesis of catalysts with catalytically active sites: it is essential for improving the catalytic performance of catalysts and understanding the catalytic mechanism. (2) Stability in strongly acidic and alkaline media: poor stability limits the wide application of catalysts in different electrolytes. (3) Large-scale production: it requires the use of low-cost raw materials and simple synthesis procedures. The emergence of MOF/PBA materials seems to be able to effectively solve the above problems. MOFs/PBAs have the advantage of strong metal ion tunability, which can regulate the active center from the atomic level, thus achieving precise synthesis of catalytic active sites. Moreover, MOFs/PBAs contain sufficient carbon sources, and the in situ generated carbon layers can effectively resist the etching of strong acid and strong alkali, so their derived catalysts can maintain excellent stability. Besides stability, due to the large specific surface areas and the uniform distribution of catalytic active sites, MOF/PBA-derived metals, alloys, metal oxides, metal sulfides, metal selenides and metal phosphides tend to exhibit superior catalytic activity [73–76]. For MOF-derived catalysts, the organic ligands are usually expensive, and the precursor syntheses is often complicated, which greatly limit their large-scale application [40]. In contrast, PBAs, representative cyanide-based coordination polymers with characteristics of low raw materials and simple synthesis, can be prepared on a large scale by simple and facile co-precipitation at room temperature [50,51]. Therefore, PBAs are ideal candidates for large-scale preparation of highly active electrocatalysts for water splitting.

In this review, we systematically summarize the most recent advances on 3d-metal-based PBAs and their derivatives as electrocatalysts for water splitting. Firstly, we discuss the synthetic strategies for PBAs and PBA-derived nanomaterials. Then, we summarize a series of characterization methods to explore the real active species of PBA and their derived nanomaterials for electrocatalytic water splitting. Subsequently, we summarize various PBAs and PBA derivatives including metals, alloys, metal oxides, metal sulfides, metal selenides and metal phosphides for electrocatalytic water splitting (HER, OER, and overall water splitting). We also deeply discuss the strategies for improving the electrocatalytic activity, such as regulating morphology, structural modification, element doping, associating conductive materials and so on. Finally, we address some existing scientific challenges and provide perspectives for the future research in the field.

2. Synthetic strategies for Prussian blue analogues and their derived nanomaterials

2.1. Synthetic strategies for PBAs

The strategies for synthesizing PBAs mainly include co-precipitation method and etching method [77–96]. The advantages and disadvantages of both methods are summarized in Table 1. The

Table 1
The methods for preparation of PBAs and PBA-derived nanomaterials.

Methods	Preparation processes	Advantages	Disadvantages
Co-precipitation (PBAs)	Mix metal ions with $K_3[M(CN)_6]$ (M = Ni, Co, Fe, etc.)	Simple and low cost	Fast nucleation leading to PBAs with irregular morphology
Etching (PBAs)	Use $K_3[M(CN)_6]$ (M = Ni, Co, Fe, etc.) to etch metal hydroxides/oxides	Effectively control the nucleation rate, resulting in well-structured PBAs	Need to prepare metal hydroxides/oxides or arrays first
Solution-phase reaction (derivatives)	React PBA precursors/ templates with S or Se sources (Na_2S, $(NH_4)_2MoS_4$, Se powder, etc.) under hydrothermal/solvothermal conditions	Low energy consumption (the reaction temperature is always less than 200 °C)	Derived catalysts have poor catalytic performance
Gas-solid reaction (derivatives)	Thermally treat PBA precursors/templates with sulfur powder, Se powder, or NaH_2PO_2 in the tube furnace under inert gas atmosphere	Obtaining highly conductive graphitized carbon; derived catalysts show excellent catalytic performance	High energy consumption (the reaction temperature usually exceeds 600 °C)

co-precipitation for preparing PBAs is usually realized by mixing metal ions with $K_3[M(CN)_6]$ (M = Fe, Co, Cr, etc.) [77–81]. The advantage of this method is simple and low-cost. The disadvantage is that in the absence of additives, the nucleation rate of PBAs is faster, resulting in PBAs with irregular shape [77]. For example, Yamauchi et al. synthesized a series of PBAs including Co-Fe PBA, Ni-Fe PBA, Ni-Co PBA, Ni-Cr PBA via mixing hexacyano-metallic complex ions with metal ions in water [78]. In a typical procedure, metal salt (nickel chloride or cobalt chloride) and sodium citrate were dissolved in water to form a clear solution of A. $K_3[M(CN)_6]$ (M = Fe, Co, Cr) was dissolved into water to form a clear solution of B. A and B were mixed under magnetic stirring until the mixture became clear. The obtained solution was aged for 24 h. The PBAs as precipitates were collected by centrifugation. They found that the PBA nucleation was rapid and the co-precipitation reaction was usually completed in a few minutes. Therefore, direct mixing of metal ions with $K_3[M(CN)_6]$ without adding sodium citrate often resulted in irregular PBA nanoparticles. The sodium-citrate-coordinated metal ions reacted slowly with $K_3[M(CN)_6]$, ensuring the slow nucleation of PBAs and controllable crystal growth, thus generating well-structured PBA nanocubes.

$K_3[M(CN)_6]$ (M = Ni, Co, Fe) can etch metals, metal oxides or metal hydroxides to fabricate PBAs [82–84], thus PBAs can also be prepared by an etching method. The reaction mechanism is that $K_3[M(CN)_6]$ etch metals, metal oxides or metal hydroxides, which release the corresponding metal ions and co-precipitate with $K_3[M(CN)_6]$ to form PBAs [82–84]. This method can effectively control the nucleation rate of PBAs, resulting in well-structured PBAs or even PBA nanoarrays [82–84]. For instance, Zhang et al. fabricated PBA nanocubes by using metal hydroxides/oxides as the precursors and templates [82]. A series of PBA nanocubes could be fabricated on cobalt oxide, manganese oxide, copper hydroxide, cobalt fluoride hydroxide, monometal or bimetal nickel-cobalt hydroxide nanosheets by etching these metal hydroxides/oxides with $K_3[M(CN)_6]$ (M = Co, Fe). Zou et al. used $K_3[Co(CN)_6]$ solution to etch nickel hydroxide nanoplate arrays and fabricated well-ordered Ni-Co PBA nanoarrays [84].

Both approaches have pros and cons. It should be noted that several reports utilized acid during the synthesis process, which produced highly toxic HCN [67]. For safety and health reasons, all synthetic experiments involving the possibility of producing HCN must be operated in fume hoods.

2.2. Preparation approaches for PBA-derived nanomaterials

2.2.1. Solution-phase reaction

Solution-phase reaction is usually used to prepare metal oxides and metal chalcogenides from PBA precursors/templates [97–100]. The advantage of the solution-phase reaction is that the reaction temperature is always less than 200 °C, so the energy consumption is low. However, the disadvantage of this method is that the prepared catalysts suffer from poor conductivity and thus exhibit poor catalytic activity. For example, Lou et al. reported an etching/anion exchange strategy for converting Ni-Co PBA nanocubes to nickel sulfide nanoframes [98]. In a typical procedure, Ni-Co PBA nanocubes were dispersed into ethanol with the assistance of ultrasonication to obtain a homogeneous suspension. Subsequently, the Na_2S aqueous solution was added to the Ni-Co PBA nanocubes suspension with continuous stirring. The resulting mixture was transferred into a Teflon lined stainless-steel autoclave and kept at 100 °C for 6 h in an electric oven. The NiS nanoframes were collected by centrifugation. Controlling the ion exchange rate between $[Co(CN)_6]^{3-}$ and S^{2-} was the key step. Excessive ion exchange would easily cause the skeleton to collapse. The addition of proper amount of ethanol could slow down the ion exchange rate. Li and coworkers reported a facile hydrothermal approach to prepare Co-doped MoS_2 nanoboxes via reacting Co-Co PBA nanocubes with $(NH_4)_2MoS_4$ [99]. Typically, Co-Co PBA nanocubes (30 mg) and $(NH_4)_2MoS_4$ (10 mg) were mixed in DMF. Then, the mixed solution was transferred into Teflon lined stainless-steel autoclave and kept at 210 °C for 12 h in an electric oven. The Co-doped MoS_2 nanoboxes were collected by centrifugation. Wang et al. prepared NiFe-based selenide through hydrothermal treatment of Ni-Fe PBA and Se powder [100]. Ni-Fe PBA was dispersed in a mixture of water and hydrazine hydrate. Subsequently, adding selenium powder to the mixed solution. The mixed solution was transferred into Teflon lined stainless-steel autoclave and heated at 180 °C for 5 h in an electric oven. Ni-Fe-Se was formed and collected by centrifugation.

2.2.2. Gas-solid reaction

Besides solution-phase reaction, gas-solid reaction is also a wide strategy used for synthesizing PBA derivatives [101–106]. Highly conductive graphite carbon can be generated in situ, and thus the derived catalysts exhibit good catalytic performance. Guo and coworkers synthesized core-shell NiFe alloy@N-doped carbon nanocages via carbonization of Ni-Fe PBA at 600 °C for 3 h under H_2/Ar atmosphere [102]. Ni-Fe PBA nanocubic precursor offered NiFe alloy and ensured in situ generation of N-doped carbon without additional N and C sources. During the thermal treatment process, Ni^{2+} and Fe^{3+} on the surface of Ni-Fe PBA were reduced by hydrogen to generate NiFe alloy. The pyrolysis of cyano ligand in situ generated nitrogen-doped graphite carbon and coated on NiFe alloy to get a core-shell material. Core-shell Fe/Fe_5C_2@N-doped carbon can also be prepared by gas-solid reaction. The thermal treatment of bimetallic Zn-Fe PBA at 1000 °C for 2 h under N_2 atmosphere yielded a Fe/Fe_5C_2@N-doped carbon core-shell material [103]. Structural studies revealed that the Fe/Fe_5C_2 core was encapsulated inside the shell of the nitrogen-doped graphite carbon. During the annealing process, metallic zinc sublimation could help to generate nanoporous structure and thus improved the homogeneous distribution of Fe/Fe_5C_2.

After the pyrolysis process, the derived nanomaterials sometimes can maintain similar morphology to that of PBAs. For example, Guo et al. successfully converted Co-Fe PBA nanocubes into hollow porous $CoFe_2O_4$ nanocubes [104], which was prepared by heating the as-prepared Co-Fe PBA precursor to 350 °C with a heating rate of 1 °C/min under air flow, and further maintained at 350 °C for 4 h. They found that the $CoFe_2O_4$ nanocubes were hollow structure rather than solid, which might be attributed to the fast mass-transport across the shells during the annealing process. PBAs can also be converted into metal chalcogenides and metal phosphides by the gas-solid reaction [105,106]. For example, Ji group synthesized $Ni_{0.67}Fe_{0.33}Se_2$ by selenization of Ni-Fe PBA at 500 °C under Ar/H_2 flow [105]. Zhao et al. prepared $Co_{0.37}Fe_{0.26}S$ and $Co_{0.4}Fe_{0.28}P$ through thermal treatment of CoFe-PBA precursor with sulfur powder and NaH_2PO_2 at 350 °C under Ar atmosphere, respectively [106].

3. Characterization of PBAs and their derived nanomaterials

Systematic characterization of PBAs and their derived nanomaterials is very important. Through scanning electron microscope (SEM), transmission electron microscopy (TEM), X-ray diffraction (XRD), X-ray photoelectron spectroscopy (XPS), X-ray absorption spectroscopy (XAS) and so on, we can reveal the morphology, crystal phase structure, element composition and content of the catalysts [101–106]. Besides, we can also evaluate the stability of catalysts by these characterization methods. The stability of catalysts is of great significance for energy conversion systems, which is one of the important parameters for evaluating the commercialization of catalysts. In particular, some catalysts may decompose or transform during an electrochemical test [105,106]. During the electrochemical process, the catalytic activity of some catalysts will become worse, and some will become better. Therefore, rigorous characterization should be made to assess the stability of the structure and confirm the active species. The characterization can guide us to synthesize catalysts with excellent catalytic performance. The SEM and TEM measurements were usually used to characterize the morphology of PBAs and their derived nanomaterials. Morphological regulation can improve the catalytic performance of the catalysts. For example, the catalysts with a small particle size, hollow or ultra-thin nanosheet structure tend to have large active specific surface areas, thus exhibiting good catalytic activity [67]. Besides, morphology change of the catalysts during the catalytic process can be observed by SEM and TEM, so as to judge the stability of the morphology of the catalysts.

XRD measurement can be performed to analyze the phase and crystalline features of PBAs and their derived nanomaterials. Through XRD, we can know what the synthesized catalyst is and determine if the species are we anticipate. In addition, we can also know the stability of the crystal phase structure of the catalyst during the catalytic process, and judge whether there is new species generated. For example, Zou et al. utilized a $K_3[Co(CN)_6]$ aqueous solution to etch nickel hydroxide. After reacting for 30 h, XRD analysis showed that the initial XRD peaks of nickel hydroxide completely disappeared, and the newly appeared peaks matched well with $Ni_3[Co(CN)_6]\cdot 12H_2O$, indicating that nickel hydroxide was completely converted into Ni-Co PBA [84].

XPS measurement was used to investigate the surface chemical compositions and element valences, by which we can analyze which elements the catalyst is composed of. Moreover, XPS was also commonly used to analyze the conversion of catalysts in the catalytic process and to determine if new species were formed. For example, Zhang et al. found that the XPS peaks of Co and Fe in Co-Fe PBA derived catalyst shifted to high binding energy and the absence of N1s peaks after the electrochemical measurement, which could be attributed to the generation of surface oxide layer [82].

The XAS measurement is a very important method to investigate the electronic and local coordination structures of PBAs and their derived nanomaterials. Soft X-ray absorption spectroscopy (s-XAS) identified the oxidation and spin states of metal elements. For example, Zhang et al. found that Ni-Fe PBA determined a 6-fold coordination structure of Ni, and Fe was coordinated with six carbon atoms from the Fourier transform extended X-ray absorption fine structure (FT-EXAFS) spectra [107]. s-XAS revealed that the Ni L-edge spectra possessed the same characteristics as NiO, indicating that Ni^{2+} is a high-spin configuration and Fe is low-spin Fe^{2+} in Ni-Fe PBA. The above results suggest that the synthesized Ni-Fe PBA electrocatalyst has a clear cubic structure.

Recent studies have shown that the MOFs, metal chalcogenides and metal phosphides are easily converted into new active species under electrochemical oxidation conditions in alkaline medium [107–110]. In situ generated active species during the OER process can greatly promote the electrocatalytic activity. To explore the real active species and further understanding the catalytic pathways, a series of characterization methods including XAS, SEM, TEM, XRD, and XPS are performed [107–110]. For example, Zhang et al. utilized Ni-Fe PBA (denoted as NF-PBA) as a model to reveal the nature active sites at the atomic level for OER [107]. They found that the fully activated electrocatalyst (denoted as NF-PBA-A) exhibited significantly enhanced catalytic performance for OER. In order to reveal the essential reasons for the improvement of catalytic activity, they systematically characterized the fully activated catalyst. The SEM and TEM images showed that initial cubic shape of NF-PBA turned into shapeless morphology. The elemental mapping of NF-PBA-A revealed that the existence and homogeneous distribution of Ni and O elements, while no Fe and N elements was detected. The XRD result confirmed that the crystalline structure of NF-PBA completely converted into an amorphous structure. X-ray absorption near edge structure (XANES) demonstrated that the in-situ generated active species had an analogous structure of $Ni(OH)_2$. Combining the above characterizations, they confirmed that the NF-PBA electrocatalyst was fully converted into a amorphous $Ni(OH)_2$ structure after OER activation in KOH. Moreover, operando X-ray spectroscopic studies suggested that $Ni(OH)_2$ deprotonated at an applied voltage to produce $NiOOH_{2-x}$ containing tetravalent nickel ions, which activated oxidized oxygen ions as electrophilic centers for OER, thus enhancing the catalytic activity. Song and coworkers also revealed that Co-Co PBA was converted to layered hydroxide-oxyhydroxide structure during the OER process [108]. They conducted detail spectroscopic and microscopic studies on the Co-Co PBA catalyst after OER. Fourier-transform infrared (FTIR) spectra and Raman tests showed that the characteristic peak of CN group in Co-Co PBA could not be detected at all after OER. XPS confirmed that PBA was converted to the hydroxide-oxyhydroxide under electrochemical oxidation. Furthermore, the SEM and TEM images revealed that initial cubic shape of Co-Co PBA converted into thin transparent nanoplates. The in situ formed hydroxide-oxyhydroxide structures offered the active sites for OER.

In addition to PBAs, PBA-derived nanomaterials, expecially metal chalcogenides and metal phosphides, can also generate new active species during electrochemical oxidation process [109,110]. For instance, Ho et al. synthesized nickel iron selenides from Ni-Fe PBA and explored the surface electronic structure of the derived catalyst after OER [109]. The XPS results revealed that the surface selenide phase was partially converted into oxyhydroxide active species. The in situ formed oxyhydroxides endowed the electrocatalyst with abundant electrocatalytic active sites, thus showing enhanced catalytic activity. Hu and coworkers prepared Fe-doped CoP catalyst from Co-Fe PBA and revealed the new generated active species after OER by XRD, XPS and TEM tests [110]. XRD showed that CoP crystal phase was completely replaced by CoOOH crystal phase after OER. XPS analysis indicated that the P element was etched away and transformed into CoOOH and FeOOH species during the OER process. In addition, the high resolution TEM (HRTEM) image showed that some new species were generated, which presented apparent lattice fringes with lattice spacing of 0.25 nm, in accordance with the interplanar spacings of the (1 0 0) crystal plane of CoOOH. The above characterizations revealed that the metal phosphide electrocatalyst was converted into metal oxyhydroxides after OER, which was the real active species for OER.

In all, PBAs and their derived metal chalcogenides and metal phosphides are easily converted into the corresponding hydroxides/oxyhydroxides during the OER process. These in-situ generated hydroxides/oxyhydroxides are real electrocatalytically active species that participate in the entire catalytic reaction. More careful and thorough characterizations to the catalysts need to be done before made a conclusion on the real catalysts.

4. PBAs for electrocatalytic water splitting

With open framework structures, large specific surface areas, adjustable metal sites and uniform catalytic centers, PBAs show promising application in electrocatalytic water splitting by themselfs [111–123]. Galán-Mascarós and coworkers reported a chemical etching approach to prepare electrochemically active Co-Fe PBA film [122]. As shown in Fig. 1, $Co(OH)_{1.0}(CO_3)_{0.5}\cdot nH_2O$ was first grown on FTO conductive substrate through a simple hydrothermal procedure. Then, $Co(OH)_{1.0}(CO_3)_{0.5}\cdot nH_2O$ on FTO was chemically etched with $K_3[Fe(CN)_6]$ to yield electrochemically active Co-Fe PBA thin film. During the etching process, $Co(OH)_{1.0}(CO_3)_{0.5}\cdot nH_2O$ served as a self-sacrificing template to provide cobalt ions, and the released cobalt ions were immediately co-deposited with excess ferricyanide ions to obtain well-formed cubic-shaped Co-Fe PBA crystals. After 3 h of etching, the nanowires completely transformed into macroporous Co-Fe PBA nanocube layers (Fig. 1e and 1f). The self-sacrificing template method could not only effectively avoid the formation of Co-Fe PBA agglomerates, but also avoid the use of an adhesive to prepare electrodes. Therefore, Co-Fe PBA thin film exhibited great electrocatalytic activity and stability for OER in a broad pH range ($1 < pH < 13$).

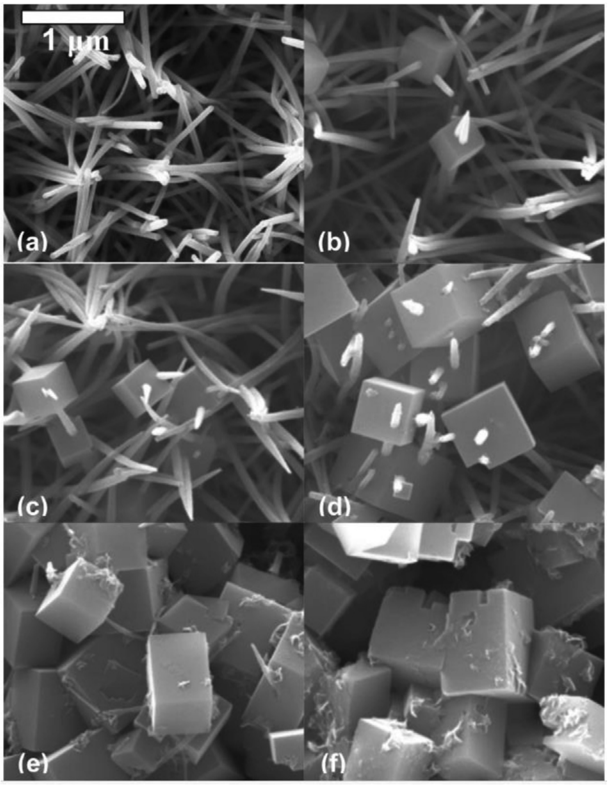

Fig. 1. Field-emission scanning electron microscopy (FESEM) images of $Co(OH)_{1.0}(CO_3)_{0.5}\cdot nH_2O$ after etching with $K_3[Fe(CN)_6]$ for (a) 0 (b) 0.5, (c) 1.0, (d) 1.5, (e) 2.0 and (f) 3.0 h. Adapted from Ref. [122].

Besides preparation of electrochemically active PBAs for OER, the external stimuli could further boost their electrocatalytic OER activity. A low-temperature air plasma strategy was very recently developed to activate the metal sites in Co-Fe PBA [123]. The treated Co-Fe PBA merely required a low overpotential of 274 mV to drive a current density of 10 mA cm^{-2} for OER in 1.0 M KOH, which was much lower than that of untreated one (334 mV). The enhanced electrocatalytic activity was attributed to two factors. One is that the active oxygen species could activate Co sites in the Co-Fe PBA after the air plasma treatment, which boosted the almost complete conversion of the oxidation state of Co(II)/Co(III) to Co(III). Trivalent cobalt possesses much better OER activity than divalent cobalt. The other is that the inserted reactive oxygen species could further regulate the redox property of cobalt sites.

5. PBA-derived nanomaterials for electrocatalytic water splitting

As discussed above, PBAs have shown good performance for electrocatalytic water splitting. However, there is still a long way for PBAs used as electrocatalysts in practical application for water splitting. The first PBAs suffered is the low electrical conductivity, which will cause low catalytic current density and thus low catalytic efficiency and high overpotentials in water splitting. The second PBAs suffered low stability. They may transform to more active species as mentioned above, but more often, they deactivated following the collapse of the framework. The PBA-derived nanomaterials can well address the above problems. They show significantly enhanced electron conductivity, electrochemical activity and stability. Therefore, the PBA-derived nanomaterials have attracted considerable attention as electracatalysts for water splitting. Tables 2–4 listed the electrocatalytic performance of PBA-derived electrocatalysts for HER, OER, and overall water splitting, respectively.

5.1. PBA-derived nanomaterials for HER

Due to the insertion of the carbon layer, the PBA-derived HER catalysts exhibit good tolerance in both acidic and alkaline media [124–136]. For instance, Li and coworkers synthesized cobalt nanoparticles wrapped in N-doped graphite carbon layer (Co@NG) by carbonization of Co-Co PBA [133]. The as-synthesized Co@NG still maintained similar morphology to Co-Co PBA. The cobalt nanoparticles showed an average size of 20 nm, which were covered by 5–16 layers of graphite carbon shell. After the acid leaching, most of the metal particles were removed, leaving a large amount of hollow graphene spheres. The as-obtained Co@NG and Co@NG-acid showed great electrocatalytic HER activity in both acidic and basic conditions.

It is well-known that graphene has good electrical conductivity and a large specific surface area, which can be used to improve the catalytic performance of the catalysts. Li et al. readily prepared a non-noble metal catalyst (Co@Co-N/rGO) for HER via thermal treatment of Co-Co PBA, graphene oxide (GO) and $g\text{-}C_3N_4$ in the existence of silica colloids [134]. The resulted Co@Co-N/rGO

Table 2
HER performance of recently reported electrocatalysts derived from PBAs.[a]

Catalysts	Mass loading (mg cm^{-2})	η at 10 mA cm^{-2} (mV)	Tafel slope (mV del^{-1})	Substrate[b]	Refs.
Co@NG-acid	0.54	200	112	GCE	[133]
Co@Co-N/rGO	0.4	180	43	GCE	[134]
FeCo	0.32	149	77	GCE	[172]
NG-NiFe@MoC$_2$	0.2	150	88	GCE	[173]
NiFe-NCs	2.2	197	130	CFP	[165]
CNBO-NSs	0.5	140	116	GCE	[166]
NCF-MOF	0.2	270[c]	114	GCE	[125]
Ni-Co-MoS$_2$	0.286	155 [d]	51	GCE	[135]
Co$_3$S$_4$@MoS$_2$	0.283	136	74	GCE	[174]
Cu-Ni-CoSe$_x$	0.668	50.2	49.6	FTO	[126]
(Ni,Co)Se$_2$-GA	2.5	128	79	NF	[175]
NiFeSe@NiSe|O	1.0	62	48.9	CF	[109]
Ni-Co-P-300	0.286	150	60.6	GCE	[127]
Ni$_2$P/NiCoP@NCCs	0.5	116	79	GCE	[128]
Fe-Co$_x$P NCs	0.286	125[d]	55	GCE	[129]
FeP NPs	0.72	115	56	GCE	[130]
FeP/GA	0.32	150	65	GCE	[131]
CoFe-Se-P 0.1 M	0.14	183.1[c]		GCE	[167]
NC-NiFeOx@NiFe-P	0.2	237	65	GCE	[168]
MoP@PC	0.24	51[d]	45	GCE	[132]
Ni-Fe-P	0.42	182	85	GCE	[169]
Ni-Fe-P nanosheets	0.2	98	50	NF	[170]
Mn$_{0.6}$Co$_{0.4}$P-rGO	2.5	54	63	CP	[171]
Co$_{0.6}$Fe$_{0.4}$P	0.27	133	61	GCE	[176]
Fe-CoP	4.2	78	92	NF	[177]
Fe-CoP HTPAs		98	90	NF	[110]
Ni$_2$P/Fe$_2$P		121	67	TF	[136]

[a] The electrolyte is 1.0 M KOH unless otherwise stated. η is the overpotential.
[b] GCE = glass carbon electrode; CFP = carbon fiber paper; NF = nickel foam; CP = carbon paper; TF = titanium foil.
[c] The electrolyte is 0.1 M KOH.
[d] The electrolyte is 0.5 M H$_2$SO$_4$.

exhibited a stacking and wrinkle layer structure, where the Co nanoparticles with a diameter of 10–50 nm were uniformly distributed in the graphite carbon layer. Co@Co-N/rGO could be used as a highly active and stable electrocatalyst for HER in 1.0 M KOH, only requiring an overpotential of 180 mV to obtain a current density of 10 mA cm^{-2} with a small Tafel slope of 43 mV dec^{-1}.

Paik and coworkers reported a PBA-engaged approach for synthesizing Ni and Co co-incorporated MoS$_2$ nanoboxes via the solvothermal reaction of Ni-Co PBA and (NH$_4$)$_2$MoS$_4$ [135]. The as-prepared Ni-Co-MoS$_2$ retained the nanocubic architecture of Ni-Co PBA with the side length of around 440 nm and the surface of the product was aggregated by ultrathin nanosheets. The ultrathin nanosheets aggregated nanoboxes exhibited good electrocatalytic activity for HER. In 0.5 M H$_2$SO$_4$ solution, Ni-Co-MoS$_2$ required an overpotential of 155 mV to obtain a current density of 10 mA cm^{-2} with a small Tafel slope of 51 mV dec^{-1}. Several aspects were concluded for the enhanced electrochemical HER performance of Ni-Co-MoS$_2$. (1) The special hollow architecture and thin MoS$_2$ nanosheet structure provided abundant surface area for catalytic reaction. (2) The edge termination architecture ensured more electrochemical activity at the edge of the catalyst. (3) The MoS$_2$ nanosheets had a wealth of defects that ensured them to expose more edge active sites. (4) The doping of metal atoms could further regulate the electronic structure of the catalyst and optimize its catalytic performance. (5) The synergistic catalytic effects of different active species in Ni-Co-MoS$_2$ could promote their HER activity.

Shen and coworkers developed a highly active HER electrocatalyst based on Ni-Fe phosphide derived from well-ordered Ni-Fe PBA nanosheet arrays [136]. The Ni-Fe phosphide exhibited excellent HER activity in both basic and acidic conditions, requiring overpotentials of 121 and 70 mV to drive a current density of 10 mA cm^{-2} in 1.0 M KOH and 0.5 M H$_2$SO$_4$, respectively. Moreover, it was found that to drive a large current density of 100 mA cm^{-2} in 0.5 M H$_2$SO$_4$ only needed a low overpotential of 266 mV. Such a high HER performance was attributed to the hierarchical structure and abundant electrocatalytic active sites, as well as bimetallic synergistic catalysis in Ni-Fe phosphide nanosheet arrays.

5.2. PBA-derived nanomaterials for OER

Compared to the PBA-derived HER electrocatalysts, their derived OER electrocatalysts have a much richer variety. Therefore, we divide them into metals and alloys, metal oxides, metal chalcogenides, metal phosphides in discussion. PBA-derived nanomaterials usually retain the porous characteristics of PBAs, and thus show large specific surface areas and uniform active sites. Moreover, the in situ generated graphite carbon can boost the conductivity and stabilize the electrocatalysts. The N doping can enhance the intrinsic activity of electrocatalysts. Therefore, these derivatives exhibited enhanced electrocatalytic performance for OER.

5.2.1. PBA-derived metals and alloys

PBA-derived metals and alloys exihibit great catalytic performance for OER [137–145]. Compared with single metal, alloys tend to exhibit better electrocatalytic performance due to the possible synergistic catalysis effect. By utilizing Fe-Ni PBAs loaded on graphene as precursors, Xu group used a microwave-assisted chemical vapor deposition (CVD)-like approach to rapidly prepare a variety of highly dispersed monolayer/few-layer nitrogen-doped graphite carbon-coated metal alloy nanoparticles [144]. The average size of the as-obtained FeNi@NC nanocrystals was 20 nm, which were uniformly distributed on RGO (Fig. 2c and 2d). The FeNi alloy was well wrapped in thin layered N-doped graphitized carbon, which was beneficial to electron conduction and thus boosted the electrocatalytic activity (Fig. 2e). Furthermore, the graphene substrate enabled the complete exposure of all active monolayer/few N-doped graphitized carbon layers (Fig. 2f). Therefore, the as-prepared FeNi@NC/graphene electrocatalyst exhibited

Table 3
OER performance of recently reported electrocatalysts derived from PBAs.[a]

Catalysts	Mass loading (mg cm^{-2})	η at 10 mA cm^{-2} (mV)	Tafel slope (mV del^{-1})	Substrate[b]	Refs.
Co_3ZnC/Co	0.344	366	81	GCE	[137]
CoFe@NC/rGO	0.8	278	52	GCE	[138]
FeNi/HNC	0.3	250	40	GCE	[139]
NiFe@NC	0.288	258	60	GCE	[141]
NiFe@CN-G	0.286	320	41	GCE	[143]
FeNi@NC/RGO	0.51	261	40	GCE	[144]
FeCoNi	0.32	288	60	GCE	[172]
NG-NiFe@MoC_2	0.2	320	31	GCE	[173]
O-NiFe@C-600	1.83	250	56.72	GCE	[145]
Co/MnO@GC-700	0.35	358	98	GCE	[146]
NiFe-NCs	2.2	271	48	CFP	[165]
CNBO-NSs	0.5	300	60	GCE	[166]
Co_3O_4	0.286	370	53	GCE	[147]
Ni-Co mixed oxide cages		380	50	GCE	[148]
$NiO/NiFe_2O_4$	1.0	303	58.5	CP	[149]
Fe-NiO	1.18	218	47	CC	[151]
$CoFe_2O_4$	1.6	266	53	NF	[150]
NCF-MOF	0.2	320[c]	49	GCE	[125]
Co_3S_4@MoS_2	0.283	280	43	GCE	[174]
c-Ti-Fe-S boxes	0.1	350	55	GCE	[153]
Co_9S_8@NC-800	0.57	302[c]	67	GCE	[154]
A-$CoS_{4.6}O_{0.6}$ PNCs	0.8	290	67	GCE	[155]
$CoSe_2$ NBs		335	54.2	GCE	[156]
Ni-Fe-Se cages	0.1	240	24	GCE	[157]
(Ni,Co)Se_2-GA	2.5	320	70	NF	[175]
NiFeSe@NiSe|O	1.0	270	63.2	CF	[109]
$(Ni_{0.62}Fe_{0.38})_2P$	0.3	290	44	GCE	[158]
CoFePi/Ni$(PO_3)_2$	1.37	213	39	CC	[159]
CoFeP		180	55	GCE	[160]
$Co_{1-x}Fe_xP$	0.3	230	51	GCE	[161]
Ni-Fe-O-P	0.42	243	50	GCE	[162]
CoFe-Se-P	0.14	210[c]	108	GCE	[167]
NC-NiFeO_x@NiFe-P	0.2	285	48	GCE	[168]
Ni-Fe-P	0.42	271	53	GCE	[169]
Ni-Fe-P nanosheets	0.2	168	75	NF	[170]
$Mn_{0.6}Co_{0.4}P$-rGO	2.5	250	65	CP	[171]
Ni-P		300	64	GCE	[163]
$Co_{0.6}Fe_{0.4}P$	0.27	298	48	GCE	[176]
Fe-CoP	4.2	190	36	NF	[177]
Fe-CoP HTPAs		230	43	NF	[110]
$Ni_2P/(NiFe)_2P(O)$ NAs		150	60	NF	[164]

[a] The electrolyte is 1.0 M KOH unless otherwise stated. η is the overpotential.
[b] CC = carbon cloth
[c] The electrolyte is 0.1 M KOH.

Table 4
Overall water splitting performance of recently reported bifunctional electrocatalysts derived from PBAs.[a]

Catalysts	Mass loading (mg cm^{-2})	Cell votage (10 mA cm^{-2} for overall water splitting) (mV)	Substrate	Refs.
NG-NiFe@MoC_2	1.0	1.53	NF	[173]
NiFe-NCs	2.2	1.67	CFP	[165]
CNBO-NSs	0.5	1.69	GCE	[166]
Co_3S_4@MoS_2	0.6	1.58	CFP	[174]
(Ni,Co)Se_2-GA	2.5	1.6	NF	[175]
NiFeSe@NiSe|O	1.0	1.56	CC	[109]
CoFe-Se-P		1.59	NF	[167]
NC-NiFeO_x@NiFe-P	1.0	1.59	NF	[168]
Ni-Fe-P	1.0	1.67	NF	[169]
Ni-Fe-P nanosheets	0.2	1.486	NF	[170]
$Mn_{0.6}Co_{0.4}P$-rGO	2.5	1.55	CP	[171]
$Co_{0.6}Fe_{0.4}P$	2.0	1.57	NF	[176]
Fe-CoP	4.2	1.49	NF	[177]
Fe-CoP HTPAs		1.59	NF	[110]

[a] The electrolyte is 1.0 M KOH.

outstanding electrocatalytic performance for OER, which demanded a low overpotential of 261 mV to drive a current density of 10 mA cm^{-2} in 1.0 M KOH, along with excellent durability for at least 120 h.

The catalytic activity of the resulted alloy can further be boosted by O_2 plasma activation. The doped O can adjust the electronic structure of catalytic active sites, enhancing the intrinsic activity of electrocatalysts. Song and coworkers utilized an O_2 plasma treatment strategy to prepare graphitized carbon encapsulated surface activated NiFe alloy (O-NiFe@C) for electrocatalytic OER [145]. The precursor Ni-Fe PBA was prepared on carbon cloth (CC) through a facile co-precipitation approach to ensure a strong

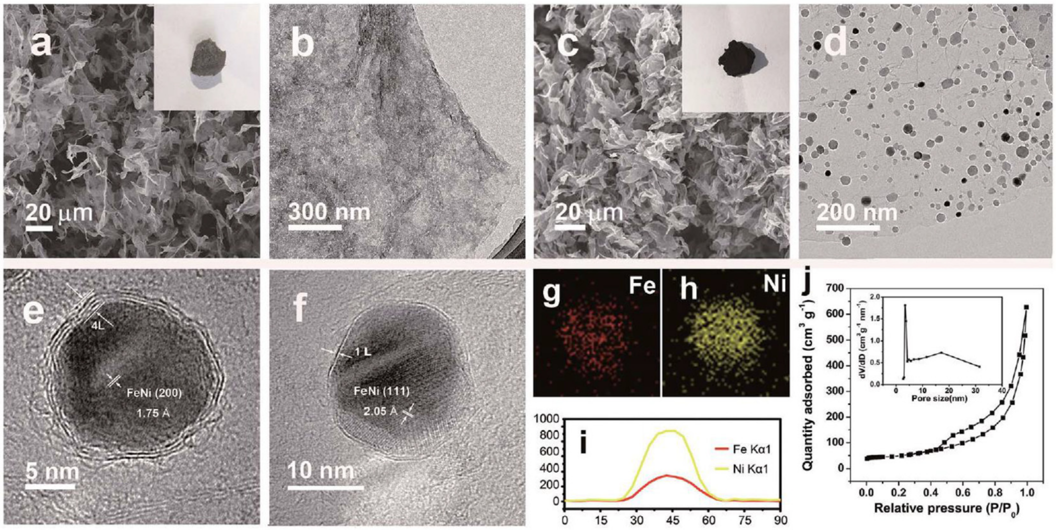

Fig. 2. (a) SEM and (b) TEM images of Ni-Fe PBA/GO. (c) SEM, (d) TEM and (e and f) HRTEM images of FeNi@NC/RGO. (g and h) EDS elemental mapping images and (i) line profiles of Fe and Ni. (j) N_2 adsorption–desorption isotherms of FeNi@NC/RGO. Adapted from Ref. [144].

connect between electrocatalyst and conductive substrate. The NiFe-PBA on CC converted into graphitized carbon encapsulated NiFe alloys (NiFe@C) through an annealing process under Ar. The reactive oxygen species were further incorporated into the surface of NiFe@C through the O_2 plasma activation. The as-prepared O-NiFe@C nanoparticles were encapsulated in layered graphite carbon shells, which exhibited outstanding electrochemical activity for OER, requiring overpotentials of 250 and 300 mV to drive the current densities of 10 and 100 mA cm^{-2} in 1.0 M KOH, respectively.

5.2.2. PBA-derived metal oxides

PBA-derived metal oxides are also significant electrocatalysts for OER [146–151]. Compared to the solid catalysts with closed-packed structures, these with porous structures are more attractive, as they have richer active specific surface areas, and the interior of the hollow structures can be fully utilized and tuned by morphology regulation. Paik et al. prepared Co_3O_4 microframes for OER by using the ammonia solution to etch Co-Co PBA microcubes and subsequent carbonization treatment [147]. After etching Co-Co PBA for 3 min, the voids inside of Co-Co PBA microcubes were formed. Extending the time to 5 min, the internal voids of the Co-Co PBA continued to increase. Further etching for 10 min, Co-Co PBA microframes were obtained by the complete transformation of Co-Co PBA microcubes. The resulted Co-Co PBA microframes were annealed at 600 °C for 2 h under air, generating well-structured Co_3O_4 microframes (Fig. 3), which exhibited great electrochemical activity for OER, demanding overpotential of 370 mV to drive a current density of 10 mA cm^{-2} in 1.0 M KOH, along with excellent durability. The enhanced electrocatalyic activity was attributed to the 3D open porous architecture, which endowed the catalyst large specific surface areas and abundant active sites.

Metal doping is a good strategy to improve the electrocatalytic performance of catalysts, as the incorporation of additional metal elements can boost the charge transfer and tune electronic structure to optimize absorbate binding energy, which in turn regulate the intrinsic electrocatalytic activity of the catalysts. For example, Lou et al. prepared Ni-Co oxide for catalytic OER by carbonization of Ni-Co PBA nanocages under air [148]. The precursor Ni-Co PBA nanocages were prepared by etching Ni-Co PBA cubes with ammonia solution. As the corners of Ni-Co PBA cubes had more defects, the etched position occurred firstly at the corner of Ni-Co PBA, and the etching rate was gradually increasing along the diagonal direction of the cube. When etched for 1 h, the solid Ni-Co PBA cubes were transformed into hollow cage-like structure. After carbonization of the Ni-Co PBA nanocages under air, Ni-Co oxide nanocages were obtained. This heterometallic Ni-Co oxide nanocages exhibited good electrochemical activity for OER, requiring an overpotential of 380 mV to drive a current density of 10 mA cm^{-2} in 1.0 M KOH.

Yoon group also studied heterometallic oxide for OER. They prepared mesoporous $NiO/NiFe_2O_4$ with hollow nanocages for OER from monodispersed Ni-Fe PBA nanocube precursor with a side length of around 200 nm [149]. The prepared $NiO/NiFe_2O_4$ hollow nanocages contained 20–30 nm shells and were composed of many nanoparticles. The unique 3D mesoporous and hollow architecture improved the electrochemically active surface area and promoted sufficient contact between the electrolyte and the electrocatalyst. Therefore, $NiO/NiFe_2O_4$ exhibited good electrochemical activity for OER, requiring a low overpotential of 303 mV to drive a current density of 10 mA cm^{-2} in 1.0 M KOH. Zhang group also developed heterometallic oxide from PBAs as electrocatalyst for OER. They converted Co-Fe PBA thin film to well-ordered porous $CoFe_2O_4$ thin film by direct carbonization [150]. The self-supporting $CoFe_2O_4$ thin film electrode exhibited great electrocatalytic activity for OER, requiring a low overpotential of 266 mV to drive a current density of 10 mA cm^{-2} in 1.0 M KOH. The $CoFe_2O_4$ thin film also exhibited excellent durability. The outstanding and stable electrocatalytic activity of $CoFe_2O_4$ thin film could be mainly attributed to the well-structured porous structure and the rich redox properties of the metal centers, which endowed the catalyst rapid charge/-electron transfer, abundant electrochemical active sites, and the well-ordered configuration of the electrode.

The catalysts with well-structured array architecture can fully expose the catalytically active sites and facilitate sufficient contact of the catalyst with the electrolyte. Therefore, growing catalysts with well-structured array architecture on a conductive substrate can further enhance the electrocatalytic activity of the catalyst. Our group reported a highly active Fe-doped NiO (Fe-NiO) electrocatalyst for OER by low temperature carbonization of a 3D Ni-Fe PBA/$Ni(OH)_2$ nanosheet arrays (Fig. 4a) [151]. The precursor Ni-Fe PBA was synthesized by a self-sacrificing template strategy, that is, $K_3[Fe(CN)_6]$ etching $Ni(OH)_2$ nanosheets released nickel ions,

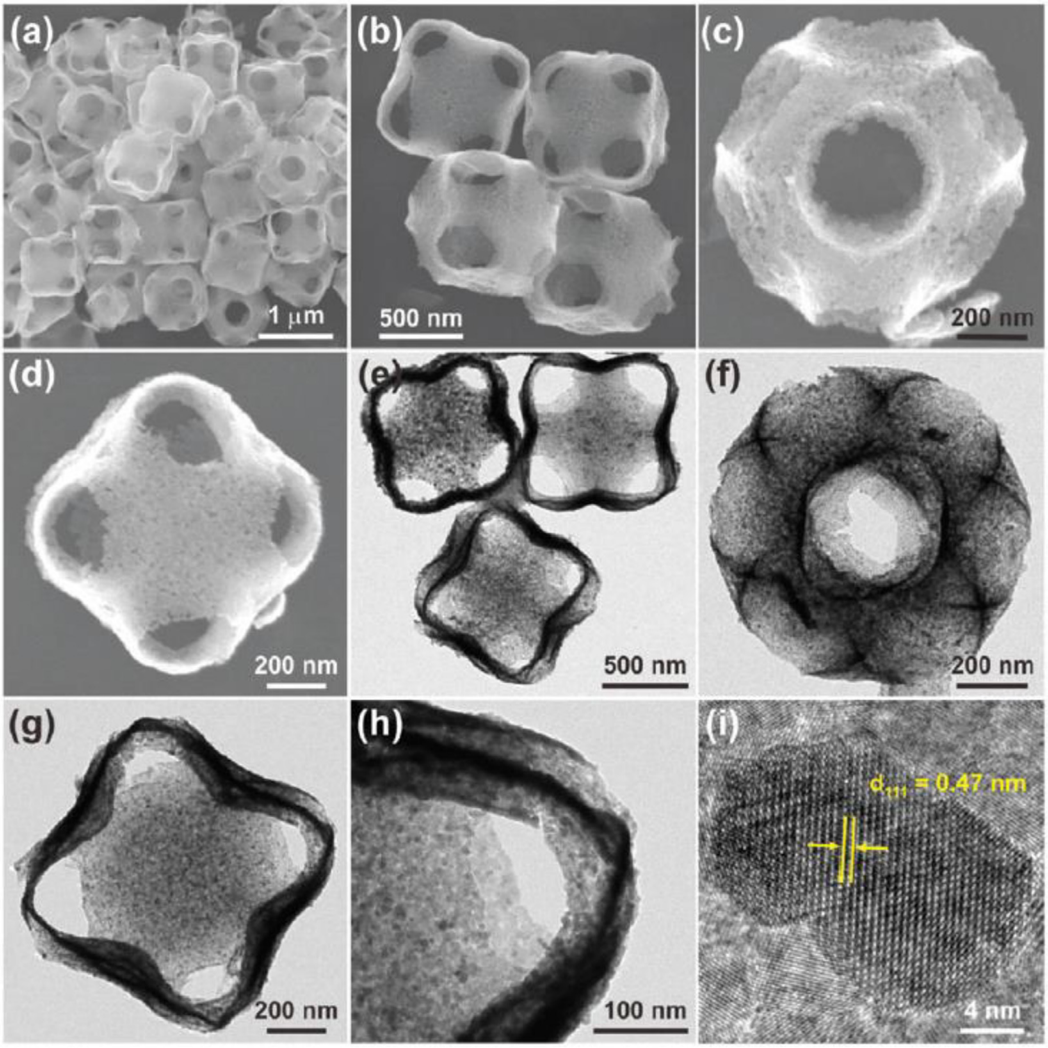

Fig. 3. SEM images (a-d) and TEM images (e-i) of Co_3O_4 microframes. Adapted from Ref. [147].

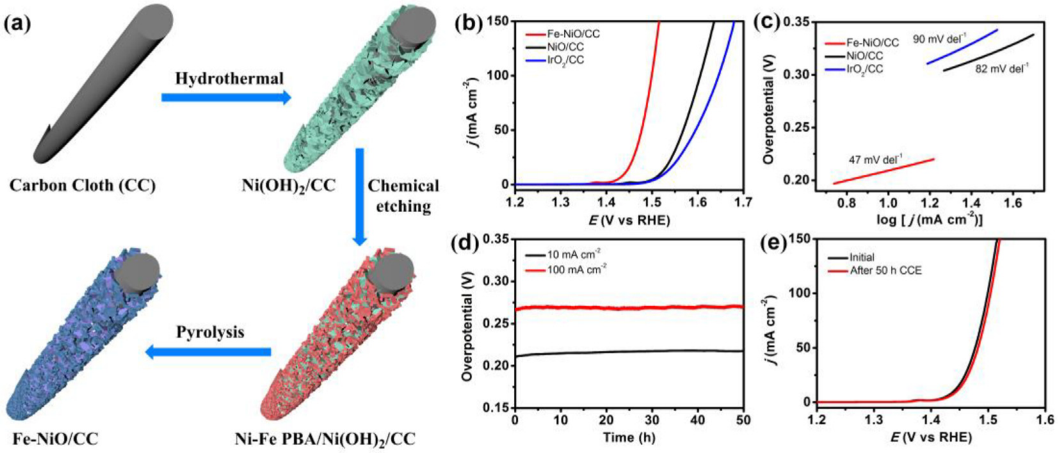

Fig. 4. (a) Schematic illustration of the preparation of porous Fe-NiO/CC electrode. (b) Linear sweep voltammetry (LSV) curves, (c) Tafel plots of Fe-NiO/CC, NiO/CC, and IrO_2/CC recorded at a scan rate of 1 mV s^{-1} in 1.0 M KOH. (d) Current density traces of Fe-NiO/CC at 10 and 100 mA cm^{-2} in 1.0 M KOH. (d) LSV curves of Fe-NiO/CC before and after OER at 10 mA cm^{-2} for 50 h. Adapted from Ref. [151].

which co-precipitated with $K_3[Fe(CN)_6]$ on the $Ni(OH)_2$ nanosheets to in situ form Ni-Fe PBA/$Ni(OH)_2$. We found that the key to obtain the well-structured template-oriented Ni-Fe PBA/$Ni(OH)_2$ nanosheet arrays was to control the reaction temperature and time. Too low reaction temperature or too short reaction time was not conducive to the growth of Ni-Fe PBA, and too high reaction temperature or too long reaction time was not benefit for the dispersion of Ni-Fe PBA on the nanosheets. The Fe-NiO electrocatalyst derived from the Ni-Fe PBA/Ni$(OH)_2$ porous nanosheet arrays exhibited excellent electrocatalytic activity and stability for OER, requiring only low overpotentials of 218 and 270 mV to drive the current densities of 10 and 100 mA cm^{-2} in 1.0 M KOH solution, respectively, and could maintain stability over 50 h electrolysis (Fig. 4b and 4d). The Tafel slope was as low as 47 mV dec^{-1}. At the overpotential of 300 mV, the TOF value reached 0.0334 s^{-1}. The highly efficient electrocatalytic performance of Fe-NiO for OER was benefited from the following aspects. Firstly, the Fe-NiO nanosheet arrays were tightly bonded to the conductive substrate, the electron conductivity of the catalyst was thus greatly improved and the working electrode was also stabilized. Secondly, the porous nanosheet array structure not only reduced the agglomeration of the catalyst and increased the electrochemically active surface area, but also facilitated sufficient contact of the electrolyte with the catalyst and release of the gas. Thirdly, the incorporation of Fe element boosted the charge transfer and regulate electronic structure to optimize absorbate binding energy, which in turn improved the electrocatalytic activity of the Fe-NiO catalyst.

5.2.3. PBA-derived metal chalcogenides

PBA-derived metal sulfides show great electrocatalytic activity for OER [152–155]. For example, Yu et al. synthesized heterometallic Ti-Fe sulfide nanoboxes for OER by a self-template approach [153]. The precursor Ti-Fe PBA nanoboxes were synthesized by a co-precipitation method and subsequent solvothermal treatment in DMF. The as-prepared Ti-Fe PBA nanoboxes were then converted into the Ti-Fe sulfide nanoboxes via vulcanization of Ti-Fe PBA in H_2S decomposed from thiourea under N_2 flow. The resulted Ti-Fe sulfide maintained the box-like structure, and exhibited nice electrochemical activity for OER, requiring an overpotential of 350 mV to drive a current density of 10 mA cm^{-2} in 1.0 M KOH, together with a small Tafel slope of 55 mV dec^{-1}.

The tuning of the electronic coupling between metal sulfide and carbon matrix also plays a significant role in improving the catalytic performance of metal sulfides. Fang et al. synthesized Co_9S_8 nanoparticles from Co-Co PBA via a simultaneous vulcanization and carbonization process [154]. A facile co-precipitation of Co^{2+} and $[Co(CN)_6]^{3-}$ in H_2O gave Co-Co PBA, which served as self-sacrificing template to fabricate Co_9S_8 nanoparticles during the sulfidation and carbonization under 5% H_2 and 95% Ar flow. The cyano group served as the carbon and nitrogen sources to form N-doped graphitized carbon to in situ encapsulate Co_9S_8 (Fig. 5). The Co_9S_8@NC exhibited good electrochemical activity and durability for OER, requiring a low overpotential of 302 mV to drive a current density of 10 mA cm^{-2} in 1.0 M KOH. Electrochemical tests and DFT calculations revealed that Co_9S_8@NC possessed great electrical conductivity and optimal oxygen adsorption free energy, which was responsible for the enhanced OER electrocatalytic performance. Additionally, the in situ generated cobalt hydroxides of Co_9S_8@NC during oxidation could also promote its OER activity.

Oxygen doping was found beneficial to improve the catalytic performance of metal sulfides, which can regulate the electronic structure of surface active sites to boost the intrinsic activity of catalysts. Wen and coworkers used ionic exchange method to prepare O-doped amorphous CoS_x porous nanocubes for OER [155]. After immersed well-ordered crystalline Co-Fe PBA nanocubes in Na_2S solution and subsequent thermal treatment at 300 °C under Ar atmosphere, A-$CoS_{4.6}O_{0.6}$ was prepared. The anionic exchange reaction endowed the resulted A-$CoS_{4.6}O_{0.6}$ with porous architecture containing abundant defect sites, thus exhibited good electrochemical activity for OER, requiring a low overpotential of 290 mV to drive a current density of 10 mA cm^{-2} in 1.0 M KOH. The Tafel slope was 67 mV dec^{-1}. In 0.1 M PBS (pH 7.0), A-$CoS_{4.6}O_{0.6}$ showed an onset overpotential of 270 mV, and requiried an overpotential of 570 mV to drive a current density of 4.59 mA cm^{-2}. DFT calculations revealed that the enhanced electrocatalytic OER activity of A-$CoS_{4.6}O_{0.6}$ was attributed to the following two aspects. One is

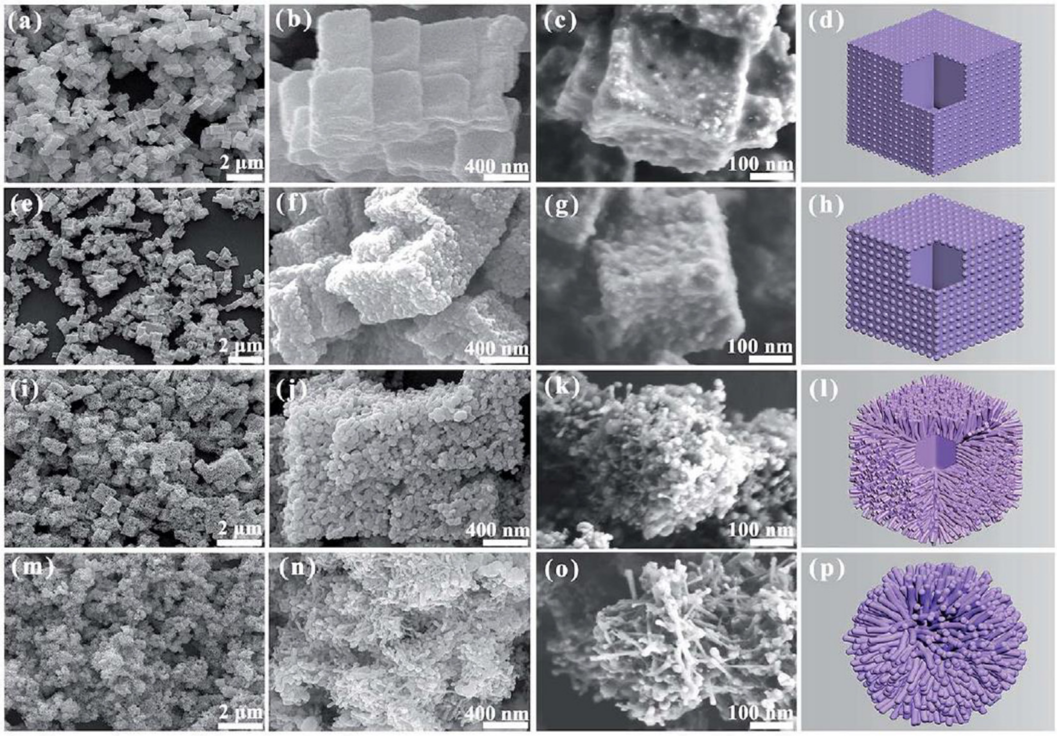

Fig. 5. SEM images of the as-obtained Co_9S_8@NC at different sulfidation temperatures (a-c) 500 °C, (e-g) 600 °C, (i-k) 700 °C, and (m-o) 800 °C. the schematics of the morphology of Co_9S_8@NC at (d) 500 °C, (h) 600 °C, (l) 700 °C, and (p) 800 °C. Adapted from Ref. [154]

that the hollow amorphous structure constructed by ultrafine nanoparticles could expose more active sites and promote catalysis, and the other is that the oxygen insertion greatly enhanced O^* adsorption, thereby enhancing the activity of a single catalytically active site.

In addition, PBA-derived metal selenides exhibit good electrocatalytic performance for OER as well [156,157]. Lou et al. employed a self-templated strategy to convert Ni-Fe PBA to metal diselenide nanocages for obtaining efficient OER electrocatalyst [157]. A co-precipitation of nickel(II) acetate tetrahydrate and potassium hexacyanoferrate(III) led to the formation of Ni-Fe PBA nanocubes, which were chemically etched in ethanol containing $NH_3{\cdot}H_2O$ (28–30%), resulting in the Ni-Fe PBA nanocages. The Ni-Fe PBA nanocages were further selenized at 350 °C for 2 h using Se powder as selenium source to obtain Ni-Fe selenide nanocages, which still maintained the original cage-like architecture, and possessed an open architecture. Ni-Fe selenide nanocages exhibited excellent electrochemical activity and nice durability for OER, demanding a low overpotential of 240 and 270 mV to drive the current densities of 10 and 100 mA cm^{-2} in 1.0 M KOH, respectively. Tafel slope was as small as 24 mV dec^{-1}. At the overpotential of 270 mV, the mass activity and turnover frequency reached as high as 1000 A g^{-1} and 0.58 s^{-1}, respectively.

5.2.4. PBA-derived metal phosphides

PBA-derived metal phosphides can usually retain the structural characteristics of PBAs, large specific surface areas and uniform distribution of active sites. Furthermore, the introduction of P can regulate the electronic structure of the catalytic center of electrocatalyst. PBA-derived metal phosphides thus exhibited excellent electrocatalytic performance for OER [158–164]. For example, Paik and coworkers reported a template-engaged approach to convert Ni-Ni PBA nanoplates to porous carbon encapsulated nickel phosphide, which was a highly active electrocatalyst for OER [163]. By phosphorization of the as-obtained Ni-Ni PBA templates at low-temperature under Ar flow afforded the Ni-P porous nanoplates, which exhibited great electrocatalytic activity for OER, requiring a low overpotential of 300 mV to drive a current density of 10 mA cm^{-2} in 1.0 M KOH. The enhanced OER performance was attributed to the following reasons. Firstly, the incorporation of the carbon layer improved the conductivity of the catalyst and stabilized the catalyst during the OER process. Secondly, the nanoporous structure ensured the catalyst exposing more catalytically active sites and facilitated sufficient contact of the electrolyte. Thirdly, the in situ generated nickel oxides/hydroxides species by Ni-P partially oxidized also contributed to the OER enhancement.

Li et al. studed the catalytic performance of Ni-Fe based catalyst as well. They constructed well-aligned O-incorporated Ni-Fe phosphide nanocube arrays on Ni foam for OER from Ni-Fe PBA [164]. $Ni(OH)_2$ nanosheet arrays were firstly grown on Ni foam by a facile hydrothermal method. Then Ni-Fe PBA was grown on the $Ni(OH)_2$ nanosheets by a gentle co-precipitation approach. After phosphorization, oxygen-incorporated $(NiFe)_2P(O)$ nanocube arrays (NAs) growing on Ni_2P nanosheets were fabricated. The $Ni_2P/(NiFe)_2P(O)$ NAs exhibited excellent electrocatalytic performance for OER, requiring overpotentials of 150 and 530 mV to obtain the current density of 10 and 800 mA cm^{-2} in 1.0 M KOH, together with excellent stability. Fantastically, even if to obtain a larger current density as high as 2000 mA cm^{-2} in 30 wt% KOH, only an overpotential as low as 400 mV was required. Systematic investigation revealed that the surface of $Ni_2P/(NiFe)_2P(O)$ was partly oxidized into amorphous Ni/Fe hydroxides and phosphates during OER process. DFT calculations demonstrated that the incorporation of iron could fabricate new catalytic active sites and form a synergistic catalytic effect with nickel. The surface oxygen doping could effectively reduce the energy barrier of intermediates and products. Moreover, the unique hierarchical nanocube arrays had a large specific surface area that could expose large amounts of catalytically active sites. Furthermore, in situ generated amorphous Ni/Fe hydroxides and phosphates could further enhance the catalytic activity and stability of the electrocatalyst.

5.3. PBA-derived nanomaterials for overall water splitting

It is very attractive to effectively drive overall water splitting by the same electrocatalyst, as it can simplify the synthesis process and reduce the overall costs [165–177]. Chen et al. systematically synthesize non-noble metals, bimetallic alloys, and ternary alloys coated in graphitized carbon layers through thermal treatment of various PBAs at 600 °C [172]. Due to the porous architecture of PBAs and the non-equilibrium mutual diffusion process of various metal atoms, the Ni, Co and Fe ions shifted to each other to generate NiCoFe alloy during the thermal treatment (Fig. 6). Meantime, the cyano group served as a carbon source and a nitrogen source to form N-doped graphitized carbon, which in situ encapsulated the metal alloy. The thickness of graphite carbon shells was about 1.71 nm, which was equivalent to 5 layers of graphene. This special structure facilitated electron conduction and the catalyst stability.

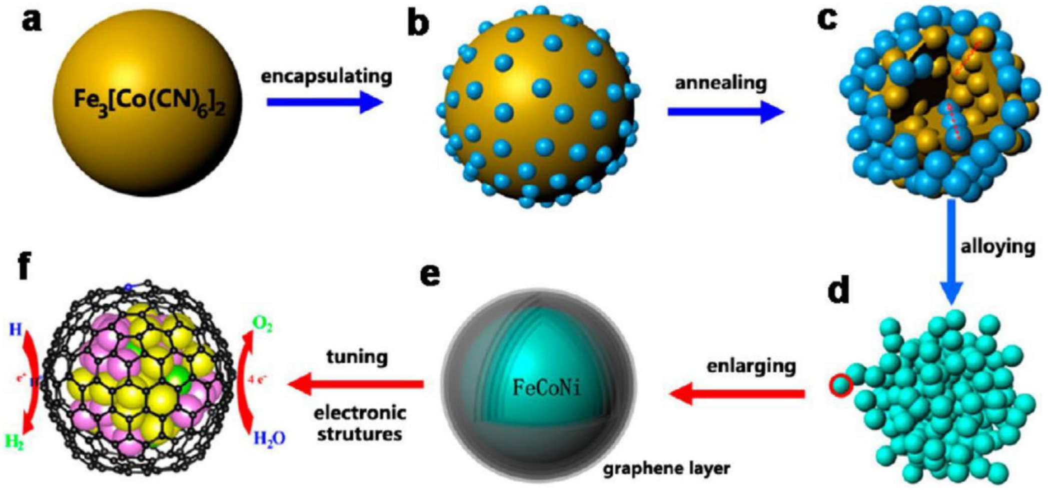

Fig. 6. Schematic illustration of the preparation of carbon-encapsulated FeCoNi ternary alloys. Adapted from Ref. [172].

For HER, the optimal electrocatalyst was FeCo alloy, which only required an overpotential of 149 mV to drive a current density of 10 mA cm^{-2} in 1.0 M KOH. For OER, the optimal electrocatalyst was FeCoNi, which required an overpotential of 288 mV to drive a current density of 10 mA cm^{-2}. Moreover, FeCo alloy and FeCoNi alloy could serve as cathode and anode to fabricate an electrolyzer for overall water splitting, showing remarkable electrocatalytic performance and stability.

By direct annealing of the mixture of PVP encapsulated Ni-Fe PBA and Mo^{6+}, Lin and coworkers prepared ultrathin N-doped graphitized carbon coated MoC$_2$-doped NiFe alloy for overall water splitting [173]. A facile co-precipitation approach was used to prepare the spherical PVP-encapsulated Ni-Fe PBA nanoparticles (Ni-Fe PBA/PVP). Then the Mo^{6+} ions were introduced into the as-obtained Ni-Fe PBA/PVP via coordination of PVP. The thermal treatment of Ni-Fe PBA/PVP/Mo^{6+} at 800 °C in Ar led to the formation of NG-NiFe@MoC$_2$. At the same time, the cyano group and PVP acted as nitrogen and carbon sources to in situ form N-doped graphitized carbon to encapsulate the alloy. As the PVP layer could significantly reduce the agglomeration of the alloy nanoparticles and dopants, MoC$_2$ could be uniformly distributed on the NiFe alloy. NG-NiFe@MoC$_2$ exhibited great electrocatalytic performance for both HER and OER, requiring overpotentials of 150 and 320 mV to obtain a current density of 10 mA cm^{-2} in 1.0 M KOH, respectively. Further studies revealed that active oxide species formed on the surface of NG-NiFe@MoC$_2$ during the OER process can boost the electrocatalytic OER activity. The NG-NiFe@MoC$_2$-based electrolyzer also showed good performance for overall water splitting, requiring a cell voltage of only 1.53 V to drive a current density of 10 mA cm^{-2}.

Morphological regulation plays an important role in boosting the catalytic performance of metal sulfides. Metal sulfide catalysts with hollow structures can make full use of their internal space, thus exhibit enhanced electrocatalytic activity. Yamauchi et al. reasonably designed a highly active and stable heterostructured Co_3S_4@MoS_2 as bifunctional electrocatalyst for both HER and OER [174]. The hollow Co_3S_4 nanoboxes were first synthesized through an ionic exchange reaction of Co-Fe PBA and S^{2-} at 120 °C in a gentle hydrothermal procedure. Subsequently, MoS_2 nanosheets were grown on the Co_3S_4 nanoboxes to obtain the heterostructured Co_3S_4@MoS_2. The synergistic catalytic effects between MoS_2 and Co_3S_4, as well as the hollow and core–shell architecture endowed Co_3S_4@MoS_2 with outstanding electrochemical activity for overall water splitting. Only overpotentials of 136 and 280 mV were needed to obtain a current density of 10 mA cm^{-2} in 1.0 M KOH for HER and OER, respectively. Moreover, the Co_3S_4@MoS_2-based electrolyzer merely required a cell voltage of 1.58 V to achieve a large current density of 10 mA cm^{-2} for overall water splitting.

Growing catalysts on the conductive carbon substrates such as graphene, carbon nanotube, carbon cloth and so on can further improve the catalyst performance, due to the fact that the introduction of the graphite carbon substrate can significantly enhance the electronic conductivity and stabilize the catalysts during the electrochemical process. Wang and coworkers covered the (Ni,Co)Se$_2$ nanocages on a 3D graphene aerogel (GA) from Ni-Co PBA precursor to get a composite electrocatalyst for overall water splitting [175]. As shown in Fig. 7a, Ni-Co PBA nanocubes were first grown on graphene oxide through a facile co-precipitation method. After a hydrothermal and freeze-drying treatment of the Ni-Co PBA-GO, Ni-Co PBA-GA was prepared, which was further selenized at 350 °C using Se powder as selenium source to afford (Ni,Co)Se$_2$-GA. The authors found that the selenization temperature had a great influence on the structure and crystal phase of the catalyst When the selenization temperature was lower than 350 °C, Ni-Co PBA could not be completely converted to selenide. When the selenization temperature was between 350 and 450 °C, Ni-Co PBA could be completely converted into selenide. When the selenization temperature was higher than 450 °C, the cubic shape of the Ni-Co PBA would be destroyed. At the optimal selenization temperature of 350 °C, the as-obtained (Ni,Co)Se$_2$ showed perfect nanocage structure containing abundant active sites. The (Ni,Co)Se$_2$-GA thus exhibited excellent electrocatalytic performance for OER,

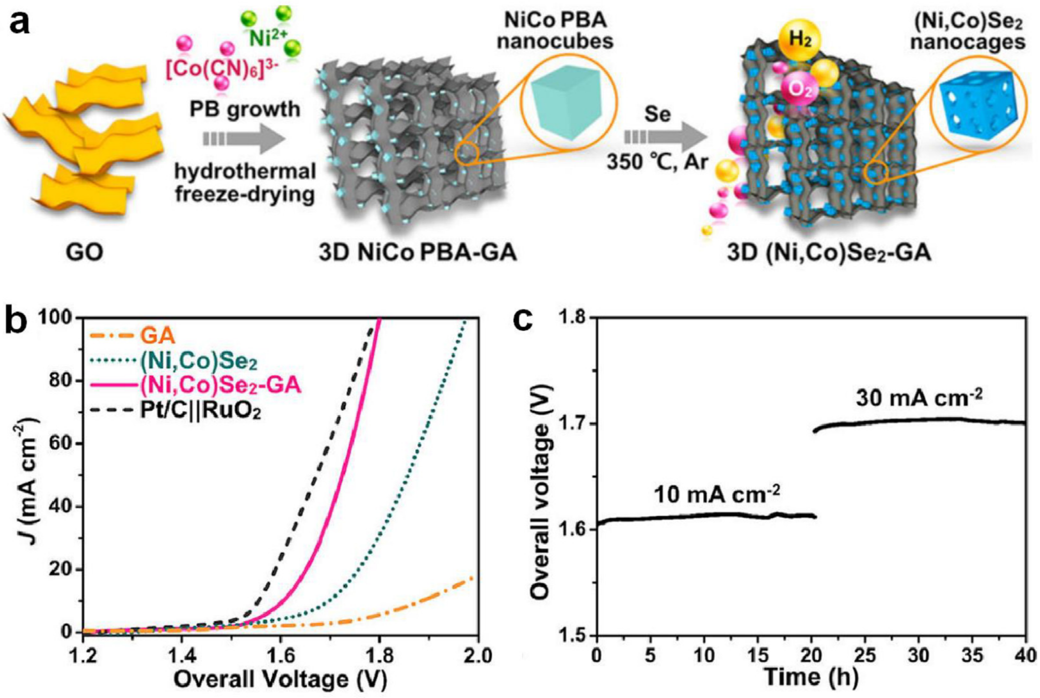

Fig. 7. (a) Schematic illustration of the preparation of (Ni,Co)Se$_2$-GA. (b) LSV curves of (Ni,Co)Se$_2$-GA in 1.0 M KOH for overall water splitting. (c) Stability tests at 10 and 30 mA cm^{-2} for overall water splitting. Adapted from Ref. [175].

demanding low overpotentials of 250 and 340 mV to drive the current densities of 10 and 100 mA cm^{-2} in 1.0 M KOH, respectively, and with a small Tafel slope of 70 mV dec^{-1}. Additionally, (Ni,Co)Se_2-GA also exhibited excellent electrocatalytic performance for HER, only requiring low overpotentials of 128 and 240 mV to drive the current densities of 10 and 100 mA cm^{-2}, respectively. The (Ni,Co)Se_2-GA-based electrolyzer merely required a cell voltage of 1.6 V to achieve a current density of 10 mA cm^{-2} for overall water splitting, along with excellent stability (Fig. 7b and 7c).

Heterometallic phosphide derived from PBAs showed good electrocatalytic water splitting as well. Peng et al. Bimetallic Co-Fe phosphide nanoframes were synthesized in turn by etching Co-Fe PBA with ammonium ions and phosphorizing (Fig. 8a) [176]. The afforded $Co_{0.6}Fe_{0.4}P$ nanoparticles with an average size of 3.5 nm were uniformly embedded in the carbon layer. It exhibited great electrocatalytic performance for both HER and OER, requiring overpotentials of 133 and 298 mV to obtain a current density of 10 mA cm^{-2} in 1.0 M KOH, respectively. Tafel slopes were 61 and 48 mV dec^{-1} for HER and OER, respectively. Furthermore, $Co_{0.6}Fe_{0.4}P$ could act as a bifunctional catalyst for electrocatalytic overall water splitting, only demanding a cell voltage of 1.57 V to drive a 10 mA cm^{-2} current density in 1.0 M KOH aqueous solution, showing excellent electrocatalytic stability (Fig. 8b and 8c). Further analysis indicated that $Co_{0.6}Fe_{0.4}P$ was oxidized in situ to generate Co-Fe oxides/hydroxides during the OER process, supporting more catalytically active sites.

Directly growing PBAs on conductive substrates can directly fabricate robust self-supporting electrodes containing porous electrocatalysts, which often show better electrochemical property. As the electrocatalysts are closely and strongly immobilized on the current collector, the integrated electrode materials are beneficial for increasing electrochemically active sites, enhancing the electron transportation, as well as stabilizing the working electrodes. Our group developed a facile and practical strategy to prepare a metal phosphide electrocatalyst (Fe-CoP) for overall water splitting from Co-Fe PBA [177]. As shown in Fig. 9a, Co-Fe PBA was first grown on commercial Ni foam (NF) via a co-precipitation approach. Then, the as-prepared Co-Fe PBA/NF was undergone direct phosphorization treatment at 400 °C for 3 h under N_2 flow, generating Fe-CoP catalyst. Fe-CoP exhibited excellent electrochemical activity for OER. In 1.0 M KOH, the Fe-CoP/NF self-supporting electrode required low overpotentials of 190, 227, 295 and 428 mV to obtain the current densities of 10, 100, 500 and 1000 mA cm^{-2}, respectively. Partially oxidization of Fe-CoP to Co(Fe) oxyhydroxide active species further boosted the catalytic activity. The Fe-CoP electrocatalyst also exhibited excellent HER activity, requiring a low overpotential of 78 mV to obtain a current density of 10 mA cm^{-2}. Excellent OER and HER activity enabled Fe-CoP to act as a highly efficient electrocatalyst for overall water splitting. The Fe-CoP-based electrolyzer showed excellent stability, and merely required a cell voltage of 1.49 V to achieve a current density of 10 mA cm^{-2} for overall water splitting (Fig. 9b and 9c). The excellent electrocatalytic performance was attributed to the following factors. On the one hand, the hierarchical-pore structure not only provided rich active sites, but also enhanced mass transfer and benefited to the release of gases and the contact of electrolyte. On the other hand, Fe-CoP was strongly immobilized on the current collector, which could effectively enhance electrochemically active sites, boost the electron transportation, and stabilize the working electrode.

6. Conclusions

This review article has summarized recent advances on PBAs and their derivatives as electrocatalysts for water splitting. The main goal in this field is to prepare high-efficiency non-precious metal-based catalysts to reduce the activation energy of electrocatalytic water splitting and improve the efficiency for overall water splitting. Firstly, the electrocatalytic performance of PBAs for water splitting has been studied. These catalysts have the advantages of simple synthesis, low cost and easy availability. However, the direct use of PBAs as electrocatalysts for water splitting suffers from shortcomings such as low electrical conductivity, low catalytic current density, low stability, and high overpotentials, which greatly limits their further developments. Compared to PBAs, the PBA-derived nanomaterials show significantly enhanced electron conductivity, electrochemical activity and stability. Therefore, the PBA-derived nanomaterials have better application potential for water splitting. Futhermore, the electrocatalytic performance of PBA-derived nanomaterials can be further improved by regulating morphology, structural modification, doping elements, associating conductive materials and so on. With these methods, we are sure new and applicable energy materials based on PBAs would appear in future.

7. Perspective

Despite much progress has been made, PBAs and their derived nanomaterials for electrocatalytic water splitting still face many challenges. (1) At present, most PBAs and PBA-derived electrocatalysts are active in alkaline electrolytes, which precludes their possible utilization in proton exchange membrane (PEM) based electrolysis cells. (2) The absence of highly active catalysts can drive large current density for overall water splitting. Catalysts that meet industrial production requirements must drive > 500 mA cm^{-2} current density for overall water splitting at low overpotentials. However, none of the currently reported PBAs and PBA-derived catalysts meets this requirement. (3) There are very few PBAs and their derivatives that combine the advantages of all performance indicators such as facile preparation, low-cost, excellent electrochemical performance including low overpotential, high catalytic current density, and high stability and so on. (4) The cataltytic mechanism of these catalysts for HER, OER, or overall water splitting needs to be further revealed. At present, the mechanism often inferred according to the catalyst structures/morphologies combining with the theoretical simulation. Actually, in situ characterization is very useful for understanding the reaction mechanism and real-time structural evolution of catalysts in electrolysis. However, in situ characterization technologies are currently lacking in water splitting. Therefore, to develop applicable catalysts with excellent performance in half-reaction of water splitting or overall water splitting, more efforts need to be further devoted. Future research work in this field may focus on the following aspects. (1) Theoretical calculations combined with in situ characterization experiments to understand the catalytic mechanism of HER and OER, thus providing theoretical guidance for the design and preparation of highly active PBAs and their derived electrocatalysts. (2) Regulating the electronic structure of the active catalytic center at the atomic level in PBAs or PAB-derived nanomaterials to improve their catalytic performance. PBAs have the characteristic of strong multi-metal adjustability. It is possible to prepare catalysts with excellent electrocatalytic performance by adjusting the total metal content and the ratio of different metals in PBAs. (3) The carbon-encapsulated material can effectively protect the catalyst from etching in a strong acidic environment, so it can precisely control the carbon content and carbon layer to encapsulate the catalyst to prepare an acid-resistant high-performance catalyst. Although PBAs can provide carbon sources, it is not rich enough to prepare a catalyst with suitable carbon contents. It is possible to combine

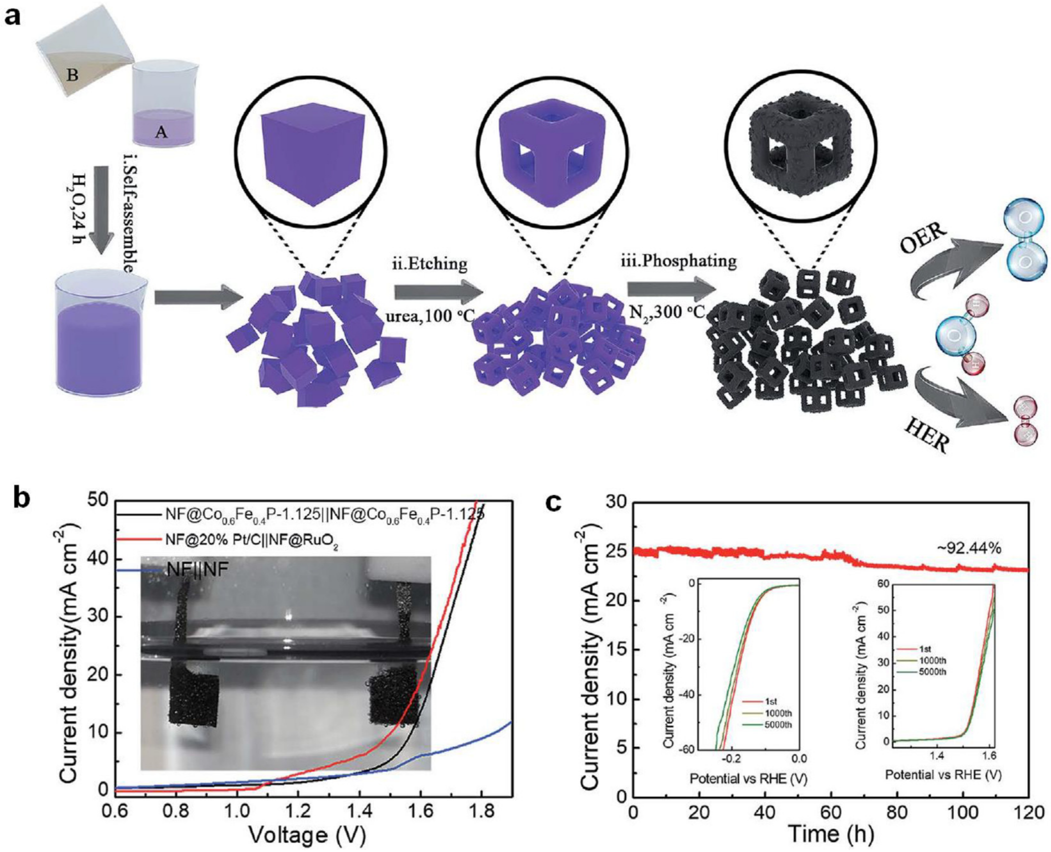

Fig. 8. (a) Schematic illustration of the preparation of $Co_{0.6}Fe_{0.4}P$. (b) The overall water splitting performance of the $Co_{0.6}Fe_{0.4}P$ and Pt/C@RuO_2 in 1.0 M KOH (inset: photo of the overall water splitting reaction in a two-electrode configuration); (c) Long-term stability test for overall water splitting (inset: the stability of $Co_{0.6}Fe_{0.4}P$ for HER and OER after 1000 and 5000 CV cycles). Adapted from Ref. [176].

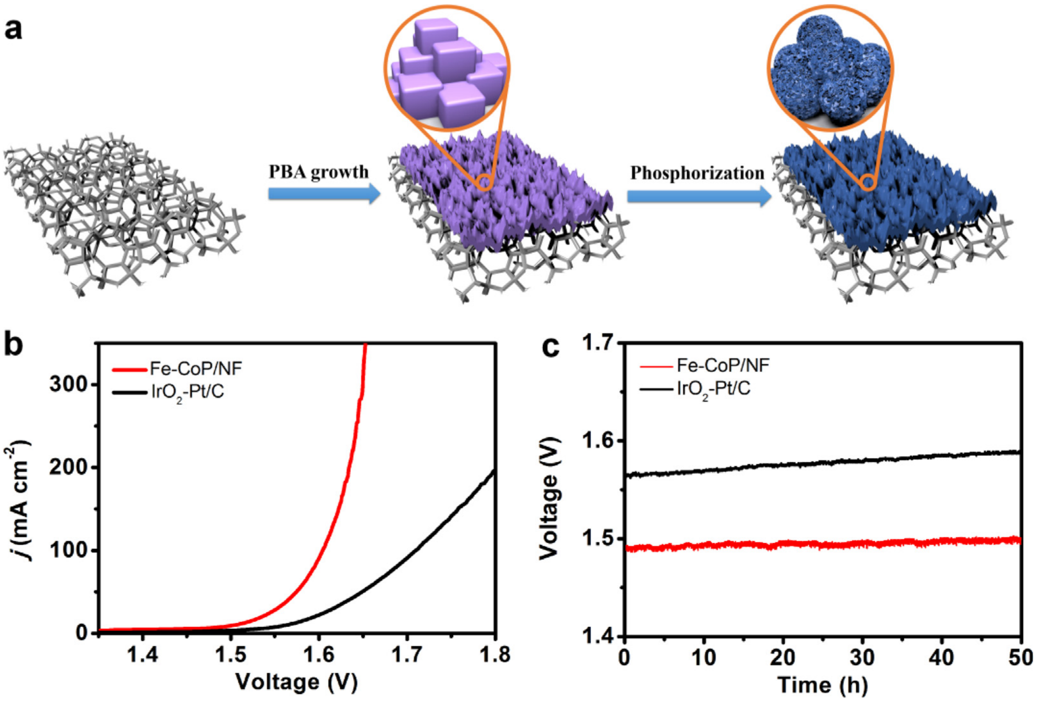

Fig. 9. (a) Schematic illustration of the preparation of porous Fe-CoP/NF electrode. (b) LSV curves of Fe-CoP/NF (red) as bifunctional catalyst in 1.0 M KOH solution for overall water splitting. IrO_2 and Pt/C as OER and HER benchmarks were measured for comparison (black). (c) Current density traces of controlled-current electrolysis at 10 mA cm^{-2} for overall water splitting in 1.0 M KOH solution. Adapted from Ref. [177]. (For interpretation of the references to colour in this figure legend, the reader is referred to the web version of this article.).

PBAs with other carbon sources (melamine, dicyandiamide, etc.) to derive the graphite carbon-coated electrocatalysts with better acid and alkali resistance, thereby improving their catalytic stability.

Declaration of Competing Interest

The authors declare that they have no known competing financial interests or personal relationships that could have appeared to influence the work reported in this paper.

Acknowledgements

This work was financially supported by the National Key R&D Program of China (2017YFA0700104), the National Natural Science Foundation of China (21931007 and 21861001, 21790052), and 111 Project of China (D17003).

References

[1] N.S. Lewis, Science 351 (2016) 1920.
[2] Y. Jiao, Y. Zheng, M. Jaroniecb, S.Z. Qiao, Chem. Soc. Rev. 44 (2015) 2060–2086.
[3] Y. Shi, B. Zhang, Chem. Soc. Rev. 45 (2016) 1529–1541.
[4] D.G. Nocera, Acc. Chem. Res. 45 (2015) 767.
[5] Y. Sun, C. Liu, D.C. Grauer, J. Yano, J.R. Long, P. Yang, C.J. Chang, J. Am. Chem. Soc. 135 (2013) 17699–17702.
[6] J. Wang, W. Cui, Q. Liu, Z. Xing, A.M. Asiri, X. Sun, Adv. Mater. 28 (2016) 215–230.
[7] Y. Yan, B.Y. Xia, B. Zhao, X. Wang, J. Mater. Chem. A 4 (2016) 17587–17603.
[8] Z.W. Seh, J. Kibsgaard, C.F. Dickens, I. Chorkendorff, J.K. Nørskov, T.F. Jaramillo, Science 355 (2017) 146.
[9] Y. Chen, K. Rui, J. Zhu, S.X. Dou, W. Sun, Chem. Eur. J. 25 (2019) 703–713.
[10] X. Zheng, B. Zhang, P.D. Luna, Y. Liang, R. Comin, O. Voznyy, L. Han, F.P. García de Arquer, M. Liu, C.T. Dinh, T. Regier, J.J. Dynes, S. He, H.L. Xin, H. Peng, D. Prendergast, X. Du, E.H. Sargent, Nat. Chem. 10 (2018) 149–154.
[11] T. Reier, Z. Pawolek, S. Cherevko, M. Bruns, T. Jones, D. Teschner, S. Selve, A. Bergmann, H.N. Nong, R. Schlogl, K.J.J. Mayrhofer, P. Strasser, J. Am. Chem. Soc. 137 (2015) 13031–13040.
[12] J.W. Wang, W.J. Liu, D.C. Zhong, T.B. Lu, Coord. Chem. Rev. 378 (2019) 237–261.
[13] J. Wang, F. Xu, H. Jin, Y. Chen, Y. Wang, Adv. Mater. 29 (2017) 1605838.
[14] H. Wang, H.W. Lee, Y. Deng, Z. Lu, P.C. Hsu, Y. Liu, D. Lin, Y. Cui, Nat. Commun. 6 (2015) 7261.
[15] A. Grimaud, O. Diaz-Morales, B. Han, W.T. Hong, Y.L. Lee, L. Giordano, K.A. Stoerzinger, M.T.M. Koper, Y. Shao-Horn, Nat. Chem. 9 (2017) 457–465.
[16] C.G. Morales-Guio, L. Liardet, X. Hu, J. Am. Chem. Soc. 138 (2016) 8946–8957.
[17] J. Bao, X. Zhang, B. Fan, J. Zhang, M. Zhou, W. Yang, X. Hu, H. Wang, B. Pan, Y. Xie, Angew. Chem. Int. Ed. 54 (2015) 7399–7404.
[18] D.Y. Wang, M. Gong, H.L. Chou, C.J. Pan, H.A. Chen, Y. Wu, M.C. Lin, M. Guan, J. Yang, C.W. Chen, Y.L. Wang, B.J. Hwang, C.C. Chen, H. Dai, J. Am. Chem. Soc. 137 (2015) 1587–1592.
[19] Y. Li, S. Chen, D. Xi, Y. Bo, R. Long, C. Wang, L. Song, Y. Xiong, Small 14 (2018) 1702109.
[20] J. Qi, W. Zhang, R. Cao, Adv. Mater. 8 (2018) 1701620.
[21] A.J. Bard, M.A. Fox, Acc. Chem. Res. 28 (1995) 141–145.
[22] T. Hisatomi, J. Kubota, K. Domen, Chem. Soc. Rev. 43 (2014) 7520–7535.
[23] M.G. Walter, E.L. Warren, J.R. McKone, S.W. Boettcher, Q. Mi, E.A. Santori, N.S. Lewis, Chem. Rev. 110 (2010) 6446–6473.
[24] G. Liu, Y. Sheng, J.W. Ager, M. Kraft, R. Xu, EnergyChem 1 (2019) 100014.
[25] T. Wang, X. Wang, Y. Liu, J. Zheng, X. Li, Nano Energy 22 (2016) 111–119.
[26] X. Wang, H. Zhang, H. Lin, S. Gupta, C. Wang, Z. Tao, H. Fu, T. Wang, J. Zheng, G. Wu, X. Li, Nano Energy 25 (2016) 110–119.
[27] T. Wang, Y. Guo, Z. Zhou, X. Chang, J. Zheng, X. Li, ACS Nano 10 (2016) 10397–10403.
[28] X. Zou, Y. Zhang, Chem. Soc. Rev. 44 (2015) 5148–5180.
[29] M. Görlin, P. Chernev, J.F. de Araújo, T. Reier, S. Dresp, B. Paul, R. Krähnert, H. Dau, P. Strasser, J. Am. Chem. Soc. 138 (2016) 5603–5614.
[30] P.Q. Liao, J.Q. Shen, J.P. Zhang, Coord. Chem. Rev. 373 (2018) 22–48.
[31] K. Wang, D. Feng, T.F. Liu, J. Su, S. Yuan, Y.P. Chen, M. Bosch, X. Zou, H.C. Zhou, J. Am. Chem. Soc. 136 (2014) 13983–13986.
[32] M. Zhao, K. Yuan, Y. Wang, G. Li, J. Guo, L. Gu, W. Hu, H. Zhao, Z. Tang, Nature 539 (2016) 76–80.
[33] Q.L. Zhu, Q. Xu, Chem. Soc. Rev. 43 (2014) 5468–5512.
[34] H. Li, L. Li, R.B. Lin, W. Zhou, Z. Zhang, S. Xiang, B. Chen, EnergyChem 1 (2019) 100016.
[35] J. Zhou, R. Li, X. Fan, Y. Chen, R. Han, W. Li, J. Zheng, B. Wang, X. Li, Energy Environ. Sci. 7 (2014) 2715–2724.
[36] X. Wang, J. Zhou, H. Fu, W. Li, X. Fan, G. Xin, J. Zheng, X. Li, J. Mater. Chem. A 2 (2014) 14064–14070.
[37] T. Wang, Q. Zhou, X. Wang, J. Zheng, X. Li, J. Mater. Chem. A 3 (2015) 16435–16439.
[38] T. Wang, R. Jin, Y. Wu, J. Zheng, X. Li, Nanoscale Horiz. 3 (2018) 218–225.
[39] Y. Guo, X. Gao, C. Zhang, Y. Wu, X. Chang, T. Wang, X. Zheng, A. Du, B. Wang, J. Zheng, K. (Ken) Ostrikovc, X. Li, J. Mater. Chem. A 7 (2019) 8129–8135.
[40] S.N. Zhao, X.Z. Song, S.Y. Song, H. Zhang, Coord. Chem. Rev. 337 (2017) 80–96.
[41] J.S. Qin, D.Y. Du, W. Guan, X.J. Bo, Y.F. Li, L.P. Guo, Z.M. Su, Y.Y. Wang, Y.Q. Lan, H.C. Zhou, J. Am. Chem. Soc. 137 (2015) 7169–7177.
[42] X.F. Lu, P.Q. Liao, J.W. Wang, J.X. Wu, X.W. Chen, C.T. He, J.P. Zhang, G.R. Li, X. M. Chen, J. Am. Chem. Soc. 138 (2016) 8336–8339.
[43] S. Zhao, Y. Wang, J. Dong, C.T. He, H. Yin, P. An, K. Zha, X. Zhang, C. Gao, L. Zhang, J. Lv, J. Wang, J. Zhang, A.M. Khattak, N.A. Khan, Z. Wei, J. Zhang, S. Liu, H. Zhao, Z. Tang, Nat. Energy 1 (2016) 16184.
[44] D. Li, H.Q. Xu, L. Jiao, H.L. Jiang, EnergyChem 1 (2019) 100015.
[45] B. Zhu, D. Xia, R. Zou, Coord. Chem. Rev. 376 (2018) 430–448.
[46] Y.Z. Chen, R. Zhang, L. Jiao, H.L. Jiang, Coord. Chem. Rev. 362 (2018) 1–23.
[47] T.Y. Ma, S. Dai, M. Jaroniec, S.Z. Qiao, J. Am. Chem. Soc. 136 (2014) 13925–13931.
[48] Y.T. Xu, X. Xiao, Z.M. Ye, S. Zhao, R. Shen, C.T. He, J.P. Zhang, Y. Li, X.M. Chen, J. Am. Chem. Soc. 139 (2017) 5285–5288.
[49] B. You, N. Jiang, M. Sheng, S. Gul, J. Yano, Y. Sun, Chem. Mater. 27 (2015) 7636–7642.
[50] L. Catala, T. Mallah, Coord. Chem. Rev. 346 (2017) 32–61.
[51] M.B. Zakaria, T. Chikyow, Coord. Chem. Rev. 352 (2017) 328–345.
[52] N.R. de Tacconi, K. Rajeshwar, Chem. Mater. 15 (2003) 3046–3062.
[53] K. Itaya, I. Uchida, Acc. Chem. Res. 19 (1986) 162–168.
[54] T. Mallah, S. Thiebaut, M. Verdaguer, P. Veillet, Science 262 (1993) 1554–1557.
[55] V. Gadet, T. Mallah, I. Castro, M. Verdaguer, J. Am. Chem. Soc. 114 (1992) 9214–9215.
[56] A.A. Karyakin, Electroanalysis 13 (2001) 813–819.
[57] S. Ferlay, T. Mallah, R. Ouahes, P. Veillet, M. Verdaguer, Nature 378 (1995) 701–703.
[58] H.J. Buser, D. Schwarzenbach, W. Fetter, A. Ludi, Inorg. Chem. 16 (1977) 2704–2710.
[59] M. Cao, X. Wu, X. He, C. Hu, Chem. Commun. 17 (2005) 2241–2243.
[60] L. Hu, J. Mei, Q. Chen, P. Zhang, N. Yan, Nanoscale 3 (2011) 4270–4274.
[61] J.L. Frisch, Miscellanea Berolinensia ad incrementum Scientiarum, 1 (1710) 377-378.
[62] A. Ludi, J. Chem. Ed. 58 (1981), 1013–1013.
[63] J.E. Chen, M.S. Fan, Y.L. Chen, Y.H. Deng, J. Ho Kim, H.R. Alamri, Z.A. Alothman, Y. Yamauchi, K.C. Ho, K.C.W. Wu, Chem. Eur. J. 23 (2017) 13284–13288.
[64] M.B. Zakaria, A.A. Belik, C.H. Liu, H.Y. Hsieh, Y.T. Liao, V. Malgras, Y. Yamauchi, K.C.W. Wu, Chem. Asian J. 10 (2015) 1457–1462.
[65] S. Pintado, S. Goberna-Ferrón, E.C.E. Adán, J.R. Galán-Mascarós, J. Am. Chem. Soc. 135 (2013) 13270–13273.
[66] H.T. Bui, N.K. Shrestha, S. Khadtare, C.D. Bathula, L. Giebeler, Y.Y. Noh, S.H. Han, A.C.S. Appl, Mater. Interfaces 2 (9) (2017) 18015–18021.
[67] J. Nai, X.W. Lou, Adv. Mater. (2018) 1706825.
[68] Y. Yang, Z. Lun, G. Xia, F. Zheng, M. He, Q. Chen, Energy Environ. Sci. 8 (2015) 3563–3571.
[69] J. Wei, Y. Feng, Y. Liu, Y. Ding, J. Mater. Chem. A 3 (2015) 22300–22310.
[70] Z. Peng, X. Qiu, Y. Yu, D. Jiang, H. Wang, G. Cai, X. Zhang, Z. Dong, Carbon 152 (2019) 16–23.
[71] R. Xiang, Y. Duan, C. Tong, L. Peng, J. Wang, S.S.A. Shah, T. Najam, X. Huang, Z. Wei, Electrochimica Acta 302 (2019) 45–55.
[72] W. Zhang, H. Zhang, R. Luo, M. Zhang, X. Yan, X. Sun, J. Shen, W. Han, L. Wang, J. Li, J. Colloid and Interface Sci. 548 (2019) 48–55.
[73] Z. Liang, R. Zhao, T. Qiu, R. Zou, Q. Xu, EnergyChem 1 (2019) 100001.
[74] Y. Du, J. Chen, L. Li, H. Shi, K. Shao, M. Zhu, ACS Sustainable Chem. Eng. 7 (2019) 13523–13531.
[75] W. Zhang, H. Song, Y. Cheng, C. Liu, C. Wang, M.A.N. Khan, H. Zhang, J. Liu, C. Yu, L. Wang, J. Li, Adv. Sci. 6 (2019) 1801901.
[76] H. Fang, T. Huang, D. Liang, M. Qiu, Y. Sun, S. Yao, J. Yu, M.M. Dinesh, Z. Guo, Y. Xia, S. Mao, J. Mater. Chem. A 7 (2019) 7328–7332.
[77] L. Deng, Z. Yang, L. Tan, L. Zeng, Y. Zhu, L. Guo, Adv. Mater. 30 (2018) 1802510.
[78] M. Hu, S. Ishihara, K. Ariga, M. Imura, Y. Yamauchi, Chem. Eur. J. 19 (2013) 1882–1885.
[79] M. Hu, N.L. Torad, Y. Yamauchi, Eur. J. Inorg. Chem. 2012 (2012) 4795–4799.
[80] J. Nai, J. Zhang, X.W. Lou, Chem 4 (2018) 1967–1982.
[81] Y. Huang, M. Xie, Z. Wang, Y. Jiang, Y. Yao, S. Li, Z. Li, L. Li, F. Wu, R. Chen, Small 14 (2018) 1801246.
[82] Y. Wang, J. Ma, J. Wang, S. Chen, H. Wang, J. Zhang, Adv. Energy Mater. 9 (2018) 1802939.
[83] B. Yuan, F. Sun, C. Li, W. Huang, Y. Lin, Electrochim. Acta 313 (2019) 91–98.
[84] Y. Shen, S.G. Guo, F. Du, X.B. Yuan, Y. Zhang, J. Hu, Q. Shen, W. Luo, A. Alsaedi, T. Hayat, G. Wen, G.L. Li, Y. Zhou, Z. Zou, Nanoscale 11 (2019) 11765–11773.
[85] W.E. Buschmann, J.S. Miller, Inorg. Chem. 39 (2000) 2411–2421.
[86] D. Aguila, Y. Prado, E.S. Koumousi, C. Mathoniere, R. Clerac, Chem. Soc. Rev. 45 (2016) 203–224.
[87] L. Ma, B. Zhou, L. Tang, J. Guo, Q. Liu, X. Zhang, Electrochimica Acta 318 (2019) 333–341.
[88] H.L. Sun, H. Shi, F. Zhao, L. Qi, Song Gao, Chem. Commun. 34 (2005) 4339–4341.
[89] X. Wang, L. Zou, H. Fu, Y. Xiong, Z. Tao, J. Zheng, X. Li, A.C.S. Appl, Mater. Interfaces 8 (2016) 8436–8444.
[90] M.V. Bennett, L.G. Beauvais, M.P. Shores, J.R. Long, J. Am. Chem. Soc. 123 (2001) 8022–8032.

[91] A. Bleuzen, C. Lomenech, V. Escax, F. Villain, F. Varret, C.C. dit Moulin, M. Verdaguer, J. Am. Chem. Soc. 122 (2000) 6648–6652.
[92] S.S. Kaye, J.R. Long, J. Am. Chem. Soc. 127 (2005) 6506–6507.
[93] T. Uemura, S. Kitagawa, J. Am. Chem. Soc. 125 (2003) 7814–7815.
[94] M. Pyrasch, A. Toutianoush, W. Jin, J. Schnepf, B. Tieke, Chem. Mater. 15 (2003) 245–254.
[95] P.A. Berseth, J.J. Sokol, M.P. Shores, J.L. Heinrich, J.R. Long, J. Am. Chem. Soc. 122 (2000) 9655–9662.
[96] N. Shimamoto, S. Ohkoshi, O. Sato, K. Hashimoto, Inorg. Chem. 41 (2002) 678–684.
[97] W.J. Li, C. Han, G. Cheng, S.L. Chou, H.K. Liu, S.X. Dou, Small 15 (2019) 1900470.
[98] X.Y. Yu, L. Yu, H.B. Wu, X.W. Lou, Angew. Chem. Int. Ed. 54 (2015) 5331–5335.
[99] G. Chen, W.F. Dong, B.L. Li, Y.H. Deng, X.H. Wang, X.F. Zhang, H.Q. Luo, N.B. Li, Electrochim. Acta 276 (2018) 81–91.
[100] C. Xuan, K. Xia, W. Lei, W. Xia, W. Xiao, L. Chen, H.L. Xin, D. Wang, Electrochim. Acta 291 (2018) 64–72.
[101] Z. Liu, Y. Wang, R. Chen, C. Chen, H. Yang, J. Ma, Y. Li, S. Wang, J. Power Sources 403 (2018) 90–96.
[102] X. Zhang, C. Li, T. Si, H. Lei, C. Wei, Y. Sun, T. Zhan, Q. Liu, J. Guo, ACS Sustainable Chem. Eng. 6 (2018) 8266–8273.
[103] L. Song, T. Wang, L. Li, C. Wu, J. He, Applied Catalysis B: Environmental 244 (2019) 197–205.
[104] H. Guo, T. Li, W. Chen, L. Liu, X. Yang, Y. Wang, Y. Guo, Nanoscale 6 (2014) 15168–15174.
[105] P. Ge, S. Li, H. Shuai, W. Xu, Y. Tian, L. Yang, G. Zou, H. Hou, X. Ji, Adv. Mater. 31 (2018) 1806092.
[106] Z. Cao, T. Zhou, W. Xi, Y. Zhao, Electrochim. Acta 263 (2018) 576–584.
[107] X. Su, Y. Wang, J. Zhou, S. Gu, J. Li, S. Zhang, J. Am. Chem. Soc. 140 (2018) 11286–11292.
[108] A. Indra, U. Paik, T. Song, Angew. Chem. Int. Ed. 57 (2018) 1241–1245.
[109] G. Yilmaz, C.F. Tan, Y.F. Lim, G.W. Ho, Adv. Energy Mater. 9 (2019) 1802983.
[110] E. Hu, J. Ning, D. Zhao, C. Xu, Y. Lin, Y. Zhong, Z. Zhang, Y. Wang, Y. Hu, Small 14 (2018) 1704233.
[111] G. Chen, W.F. Dong, Y.H. Deng, B.L. Li, X.L. Li, H.Q. Luo, N.B. Li, Chem. Commun. 54 (2018) 11044–11047.
[112] X. Zhang, P. Liu, Y. Sun, T. Zhan, Q. Liu, L. Tang, J. Guo, Y. Xia, Inorg. Chem. Front. 5 (2018) 1683–1689.
[113] H.T. Bui, D.Y. Ahn, N.K. Shrestha, M.M. Sung, J.K. Lee, S.H. Han, J. Mater. Chem. A 4 (2016) 9781–9788.
[114] B. Rodriguez-Garcia, A. Reyes-Carmona, I. Jimenez-Morales, M. Blasco-Ahicart, S. Cavaliere, M. Dupont, D. Jones, J. Roziere, J.R. Galan-Mascaros, F. Jaouen, Sustainable Energy Fuels 2 (2018) 589–597.
[115] N.K.A. Venugopal, J. Joseph, J. Power Sources 305 (2016) 249–258.
[116] A.V.N. Kumar, J. Joseph, Electrochim. Acta 139 (2014) 88–95.
[117] L. Huang, X. Ge, S. Dong, RSC Adv. 7 (2017) 32819–32825.
[118] E.P. Alsac, E. Ülker, S.V.K. Nune, Y. Dede, F. Karadas, Chem. Eur. J. 24 (2018) 4856–4863.
[119] M. Aksoy, S.V.K. Nune, F. Karadas, Inorg. Chem. 55 (2016) 4301–4307.
[120] J. Liu, S. Wei, N. Li, L. Zhang, X. Cui, Electrochim. Acta 299 (2019) 575–581.
[121] L. Zhang, T. Meng, B. Mao, D. Guo, J. Qin, M. Cao, RSC Adv. 7 (2017) 50812–50821.
[122] L. Han, P. Tang, Á. Reyes-Carmona, B. Rodríguez-García, M. Torréns, J.R. Morante, J. Arbiol, J.R. Galan-Mascaros, J. Am. Chem. Soc. 138 (2016) 16037–16045.
[123] Y. Guo, T. Wang, J. Chen, J. Zheng, X. Li, K. Ostrikov, Adv. Energy Mater. 8 (2018) 1800085.
[124] B. Rezaei, A.R.T. Jahromi, A.A. Ensafi, Electrochim. Acta 283 (2018) 1359–1365.
[125] W. Ahn, M.G. Park, D.U. Lee, M.H. Seo, G. Jiang, Z.P. Cano, F.M. Hassan, Z. Chen, Adv. Funct. Mater. 28 (2018) 1802129.
[126] Y. Niu, X. Qian, C. Xu, H. Liu, W. Wu, L. Hou, Chem. Eng. J. 357 (2019) 11–20.
[127] Y. Feng, X.Y. Yu, U. Paik, Chem. Commun. 52 (2016) 1633–1636.
[128] L. Han, T. Yu, W. Lei, W. Liu, K. Feng, Y. Ding, G. Jiang, P. Xu, Z. Chen, J. Mater. Chem. A 5 (2017) 16568–16572.
[129] X. Guo, X. Yu, Z. Feng, J. Liang, Q. Li, Z. Lv, B. Liu, C. Hao, G. Li, ACS Sustainable Chem. Eng. 6 (2018) 8150–8158.
[130] X. Zhu, M. Liu, Y. Liu, R. Chen, Z. Nie, J. Li, S. Yao, J. Mater. Chem. A 4 (2016) 8974–8977.
[131] A.V.N. Kumar, S. Yin, Y. Li, H. Xue, Y. Xu, X. Li, H. Wang, L. Wang, Chem. Asian J. 13 (2018) 679–685.
[132] S. Han, Y. Feng, F. Zhang, C. Yang, Z. Yao, W. Zhao, F. Qiu, L. Yang, Y. Yao, X. Zhuang, X. Feng, Adv. Funct. Mater. 25 (2015) 3899–3906.
[133] M. Zeng, Y. Liu, F. Zhao, K. Nie, N. Han, X. Wang, W. Huang, X. Song, J. Zhong, Y. Li, Adv. Funct. Mater. 26 (2016) 4397–4404.
[134] D. Zhao, J. Dai, N. Zhou, N. Wang, X. Peng, Y. Qu, L. Li, Carbon 142 (2019) 196–205.
[135] X.Y. Yu, Y. Feng, Y. Jeon, B. Guan, X.W. Lou, U. Paik, Adv. Mater. 28 (2016) 9006–9011.
[136] Y. Ge, P. Dong, S.R. Craig, P.M. Ajayan, M. Ye, J. Shen, Adv. Energy Mater. 8 (2018) 1800484.
[137] J. Su, G. Xia, R. Li, Y. Yang, J. Chen, R. Shi, P. Jiang, Q. Chen, J. Mater. Chem. A 4 (2016) 9204–9212.
[138] F. Kong, K. Chen, S. Song, D. Xue, Inorg. Chem. Front. 5 (2018) 1962–1966.
[139] B.K. Barman, K.K. Nanda, Green Chem. 18 (2016) 427–432.
[140] H. Wu, M. Zeng, Z. Li, X. Zhu, C. Tian, C. Xia, L. He, S. Dai, Sustainable Energy Fuels 3 (2019) 136–141.
[141] L. Dua, L. Luo, Z. Feng, M. Engelhard, X. Xie, B. Han, J. Sund, J. Zhang, G. Yin, C. Wang, Y. Wang, Y. Shao, Nano Energy 39 (2017) 245–252.
[142] Y. Zeng, G.F. Chen, Z. Jiang, L.X. Ding, S. Wang, H. Wang, J. Mater. Chem. A 6 (2018) 15942–15946.
[143] C. Deng, K.H. Wu, J. Scott, S. Zhu, R. Amal, D.W. Wang, ChemElectroChem 5 (2018) 732–736.
[144] F. Bu, W. Chen, J. Gu, P.O. Agboola, N.F. Al-Khalli, I. Shakir, Y. Xu, Chem. Sci. 9 (2018) 7009–7016.
[145] Y. Feng, H. Han, K.M. Kim, S. Dutta, T. Song, J. Catal. 369 (2019) 168–174.
[146] J. Xu, H. Zhang, P. Xu, R. Wang, Y. Tong, Q. Lu, F. Gao, Nanoscale 10 (2018) 13702–13712.
[147] Y. Feng, X.Y. Yu, U. Paik, Chem. Commun. 52 (2016) 6269–6272.
[148] L. Han, X.Y. Yu, X.W. Lou, Adv. Mater. 28 (2016) 4601–4605.
[149] B.K. Kang, M.H. Woo, J. Lee, Y.H. Song, Z. Wang, Y. Guo, Y. Yamauchi, J.H. Kim, B. Lim, D.H. Yoon, J. Mater. Chem. A 5 (2017) 4320–4324.
[150] S. Lei, Q.H. Li, Y. Kang, Z.G. Gu, J. Zhang, Applied Catalysis B: Environmental 245 (2019) 1–9.
[151] L.M. Cao, Y.W. Hu, D.C. Zhong, T.B. Lu, ChemSusChem 11 (2018) 3708–3713.
[152] Q. Hu, G. Li, X. Liu, B. Zhu, G. Li, L. Fan, X. Chai, Q. Zhang, J. Liu, C. He, J. Mater. Chem. A 7 (2019) 461–468.
[153] J. Nai, Y. Lu, X.Y. Yu, J. Mater. Chem. A 6 (2018) (1895) 21891–21892.
[154] Z. Chen, R. Wu, M. Liu, Y. Liu, S. Xu, Y. Ha, Y. Guo, X. Yu, D. Sun, F. Fang, J. Mater. Chem. A 6 (2018) 10304–10312.
[155] P. Cai, J. Huang, J. Chen, Z. Wen, Angew. Chem. Int. Ed. 56 (2017) 4858–4861.
[156] V. Ganesan, J. Kim, Mater. Lett. 223 (2018) 49–52.
[157] J. Nai, Y. Lu, L. Yu, X. Wang, X.W. Lou, Adv. Mater. 29 (2017) 1703870.
[158] H.H. Zou, C.Z. Yuan, H.Y. Zou, T.Y. Cheang, S.J. Zhao, U.Y. Qazi, S.L. Zhong, L. Wang, A.W. Xu, Catal, Sci. Technol. 7 (2017) 1549–1555.
[159] D.C. Liu, L.M. Cao, Z.M. Luo, D.C. Zhong, J.B. Tan, T.B. Lu, J. Mater. Chem. A 6 (2018) 24920–24927.
[160] X. Zhang, Y. Wu, Y. Sun, Q. Liu, L. Tang, J. Guo, Inorg. Chem. Front. 6 (2019) 604–611.
[161] Z. Li, T.T. Zhao, W.J. Jiang, S. Niu, M. Wu, J.S. Hu, A.C.S. Appl, Mater. Interfaces 10 (2018) 35904–35910.
[162] C. Xuan, J. Wang, W. Xia, J. Zhu, Z. Peng, K. Xia, W. Xiao, H.L. Xin, D. Wang, J. Mater. Chem. A 6 (2018) 7062–7069.
[163] X.Y. Yu, Y. Feng, B. Guan, X.W. Lou, U. Paik, Energy Environ. Sci. 9 (2016) 1246–1250.
[164] W. Xi, G. Yan, Z. Lang, Y. Ma, H. Tan, H. Zhu, Y. Wang, Y. Li, Small 14 (2018) 1802204.
[165] A. Kumar, S. Bhattacharyya, A.C.S. Appl, Mater. Interfaces 9 (2017) (1915) 41906–41914.
[166] T. He, J.M.V. Nsanzimana, R. Qi, J.Y. Zhang, M. Miao, Y. Yan, K. Qi, H. Liu, B.Y. Xia, J. Mater. Chem. A 6 (2018) 23289–23294.
[167] L. He, B. Cui, B. Hu, J. Liu, K. Tian, M. Wang, Y. Song, S. Fang, Z. Zhang, Q. Jia, A.C.S. Appl, Energy Mater. 1 (2018) 3915–3928.
[168] Q. Hu, X. Liu, C. Tang, L. Fan, X. Chai, Q. Zhang, J. Liu, C. He, Sustainable Energy Fuels 2 (2018) 1085–1092.
[169] C. Xuan, J. Wang, W. Xia, Z. Peng, Z. Wu, W. Lei, K. Xia, H.L. Xin, D. Wang, A.C.S. Appl, Mater. Interfaces 9 (2017) 26134–26142.
[170] C. Xuan, Z. Peng, K. Xia, J. Wang, W. Xiao, W. Lei, M. Gong, T. Huang, D. Wang, Electrochim. Acta 258 (2017) 423–432.
[171] X. Xu, H. Liang, G. Tang, Y. Hong, Y. Xie, Z. Qi, B. Xua, Z. Wang, Nanoscale Adv. 1 (2019) 177–183.
[172] Y. Yang, Z. Lin, S. Gao, J. Su, Z. Lun, G. Xia, J. Chen, R. Zhang, Q. Chen, ACS Catal. 7 (2017) 469–479.
[173] Q. Hua, X. Liu, B. Zhu, L. Fan, X. Chai, Q. Zhang, J. Liu, C. He, Z. Lin, Nano Energy 50 (2018) 212–219.
[174] Y. Guo, J. Tang, Z. Wang, Y.M. Kang, Y. Bando, Y. Yamauchi, Nano Energy 47 (2018) 494–502.
[175] X. Xu, H. Liang, F. Ming, Z. Qi, Y. Xie, Z. Wang, ACS Catal. 7 (2017) 6394–6399.
[176] Y. Lian, H. Sun, X. Wang, P. Qi, Q. Mu, Y. Chen, J. Ye, X. Zhao, Z. Deng, Y. Peng, Chem. Sci. 10 (2019) 464–474.
[177] L.M. Cao, Y.W. Hu, S.F. Tang, A. Iljin, J.W. Wang, Z.M. Zhang, T.B. Lu, Adv. Sci. 5 (2018) 1800949.